Fall 2016

Modification of the Fundamental Properties of Light Through Interaction with Nanostructured Materials

David W. Keene II

TRANSFORMATION OF THE FUNDAMENTAL PROPERTIES OF LIGHT
THROUGH INTERACTION WITH NANOSTRUCTURED MATERIALS

by

DAVID W KEENE

(Under the Direction of Maxim Durach)

ABSTRACT

The field of photonics has been growing rapidly over the last few decades as it has endeavored to harness the potential of nanostructured materials to utilize the energy and momentum of electromagnetic radiation on the nanoscale. Using metal nanostructures provides the ability to take advantage of the sub-field of plasmonics which holds the promise of opening the world to vast increases in computational power by circumventing the limitations of conventional current that plague today's processors. With a thorough understanding of this subject we also get one step closer to increasing the efficiency of solar technology, developing a finer scale of sensing technology, and a new area of minute scale mechanical manipulation of materials. There is still much work to be done before we attain these lofty goals. As such, here we present another step in the never ending journey of exploration.

INDEX WORDS: Metamaterial, Plasmon, Wave plate, Polarization, Nanotechnology, Photonics

TRANSFORMATION OF THE FUNDAMENTAL PROPERTIES OF LIGHT
THROUGH INTERACTION WITH NANOSTRUCTURED MATERIALS

by

DAVID KEENE

B.S., Georgia Southern University, 2014

A Dissertation Submitted to the Graduate Faculty of Georgia Southern University in Partial
Fulfillment of the Requirements for the Degree

MASTER OF SCIENCE

STATESBORO, GEORGIA

TRANSFORMATION OF THE FUNDAMENTAL PROPERTIES OF LIGHT
THROUGH INTERACTION WITH NANOSTRUCTURED MATERIALS

by

DAVID KEENE

Major Professor: Maxim Durach

Committee: Clayton Heller
                 Xiao Jun Wang
                 Li Ma

Electronic Version Approved:

May 2016

Acknowledgements

I would like to take this opportunity to thank the thesis committee for their support and feedback. I would also like to thank Dr. Maxim Durach specifically for his mentorship, friendship, and ceaseless patience over the last several years as he pushed me to achieve academic heights of which I never thought I was capable. Likewise, I would like to thank the entirety of the faculty and staff of the Physics department at Georgia Southern University for all of their support and encouragement. I also owe a debt of gratitude to my colleagues in the MSAPS program Grayson Wiggins, Stephanie Canonico-May, Gil Salizar, and Kelsey Almond whose help with the Chemistry material covered in some of the required classes for this program was invaluable. Lastly, I would like to thank my parents for believing in me and always pushing me to be better.

TABLE OF CONTENTS

LIST OF FIGURES

Chapter 1

Introduction

In this thesis we consider several typical situations that occur or can potentially occur in realistic nanostructures. We are trying to investigate the modifications that the presence of a nanostructure brings to the states of the optical fields with particular interest toward introducing new opportunities for optical focusing, imaging, polarization conversion etc. We are also interested in the change of the state of motion of nanostructures due to their interaction with electromagnetic fields. First, we consider how dipole radiation can be fed entirely into the near-field of a metal film if the dipole is placed within 10 nm from the film, as opposed to the far-field dipole emission in free space. This happens because the power which would be emitted into the far-field by a free-standing dipole, is consumed in the near-field due to a strong coupling of the dipole to its image dipole in the metal film via high-frequency quasi-static potential interaction. This signifies that the mere presence of a metal nanostructure can entirely switch the energy channels for the radiation of quantum emitters.

We further consider another example of a similarly drastic manipulation of light using a metal nanostructure. We show that just a 30-nm-thick metal nanowire array can swap the linear polarization of photons passing normally through it. At the same time, our estimation of the angular momentum change of the passing photons shows that the recoil from this change is enough to spin this small-moment-of-inertia nanostructure at a high rate. This makes the idea of an optical torque wrench which was proposed to monitor the rotational states of microscopic biological objects practical with plasmonic metal nanostructures. This opens up opportunities to take advantage of using the rotational plasmonic platforms with the ability of repositioning the plasmonic optical hotspots in space by the mechanical motion of nanostructures.

The theoretical groundwork for understanding electromagnetic phenomena was laid out by Coulomb, Gauss, Faraday and Ampere in the form of equations that bear their names. In 1865 James Clerk Maxwell discovered the displacement current and correspondingly introduced the notion of dielectric permittivity, which is at the core of the field of photonics. In their purest form, the Maxwell equations are a system of two equations with four variables as follows:

$$\nabla \times \vec{E} + \frac{1}{c}\frac{\partial \vec{B}}{\partial t} = 0 - \text{the Faraday's law} \qquad (1.1)$$

$$\nabla \times \vec{H} - \frac{1}{c}\frac{\partial \vec{D}}{\partial t} = \frac{4\pi}{c}\vec{j} - \text{the Ampere's law} \qquad (1.2)$$

From Ampere's law above, one can derive Gauss's law and from there Coulomb's law, so the impact of Maxwell's correction to Ampere's law cannot be overstated. In its most familiar pre-Maxwell form Ampere's law is known to be

$$\oint \vec{B} \cdot d\vec{l} = \frac{4\pi}{c}\vec{I} \qquad (1.3)$$

The necessity of Maxwell's correction to this law becomes apparent when it is applied to a capacitor. As a matter of simplicity the surface enclosed by the path that is integrated over is usually taken as a plane normal to the conductor passing through it. This need not be the case as

the path is independent of the surface it circumscribes. It is perfectly correct to extend the surface that defines the circuital path out and through the space between the plates of a parallel plate capacitor as shown below[1].
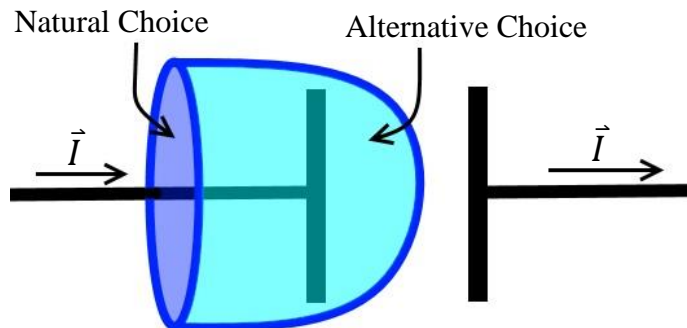

Fig. 1.1 The conflicting choices for the bounding surface when considering
Ampere's Law for a capacitor in a DC circuit

Doing so shows the flaw in Ampere's formulation. There is obviously no current flowing through the surface in this case. So, has the magnetic field just disappeared because of a choice made by the investigator? Of course not. There must be some way to reformulate Ampere's law such that this arbitrary choice still produces a correct value. To do so we must look closer at the nature of the parallel plate capacitor. Incoming current deposits charges on the first plate of the capacitor, the electric field emanating from this accumulated charge repulses like charges from the opposing plate which is then carried through the remaining circuit as current. This being the case, an analogous relationship may be drawn between current and the dynamics that facilitate the continuing current flow on the opposite side of the capacitor. The accumulation of charge in a capacitor is known to be given by

$$Q(t) = \frac{\varepsilon}{4\pi} \oiint \vec{E}(t) \cdot d\vec{S} \tag{1.4}$$

where ε is the dielectric permittivity of the material within the gap between the plates of the capacitor. Current being the flow of charge, it is proper to take the time derivative giving

$$\frac{\partial Q}{\partial t} = \frac{\varepsilon}{4\pi} \oiint \frac{\partial \vec{E}}{\partial t} \cdot d\vec{S} \tag{1.5}$$

Were we to then pose Ampere's law as a function of current density rather than current we would have

$$\oint \vec{B} \cdot dl = \frac{4\pi}{c} \oiint \vec{J} \cdot d\vec{S} \tag{1.6}$$

Now it becomes clear that the previously formed analogous formulation of current can be added to make the law whole and complete.

$$\oint \vec{B} \cdot dl = \frac{4\pi}{c} \oiint \left(\vec{j} + \frac{\varepsilon}{4\pi} \frac{\partial \vec{E}}{\partial t} \right) \cdot d\vec{S} \tag{1.7}$$

Maxwell called this additional term the displacement current density

$$\frac{\partial \vec{D}}{\partial t} \equiv \varepsilon \frac{\partial \vec{E}}{\partial t} \tag{1.8}$$

And thus the first of the material equations needed to fully solve Maxwell's equations was given.

$$\vec{D} = \varepsilon \vec{E} \tag{1.9}$$

In 1964 Dr. Victor Georgievich Veselago published a paper that would inspire the burgeoning photonics community to look in a whole new direction and guide the evolution of metamaterials for generations. He showed that if a material could be found in which both the dielectric permittivity and the magnetic permeability were less than zero that material would act in strange and wonderful new ways. Through a close examination of Maxwell's equations he established that such a material would constitute what he called a "left-handed substance." One of the consequences of this left-handedness is that the Poynting vector $(\vec{S})$ and the wave vector $(\vec{k})$ of a propagating wave would point in opposite directions. That is to say that while the phase velocity of the wave remains positive, the group velocity is negative. Dr. Veselago went on to examine the boundary conditions at the interface between a traditional "right-handed" material and his new "left-handed" one. He established that the refracted wave propagating through the "left-handed" material experienced refraction at a negative angle as shown below. This negative refraction angle would lead to the eventual introduction of the idea of a negative index of refraction[2].
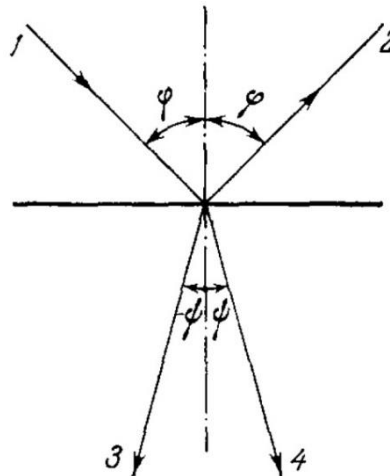

Fig. 1.2 Veselago's depiction of light interacting with the boundary of his "left-handed" material compared to a traditional "right handed" material. Ray 1 denotes the incident wave; ray 2, the reflected wave; ray 3, the wave refracted through the "left-handed" material; ray 4, the wave refracted through the traditional material. Reproduced from Ref. [2].

Fast forward to 2000 when Dr. John Pendry followed Dr. Veselago's train of thought farther than anyone thought it would go. Through the careful consideration of Fresnel's coefficients and by taking the appropriate limits for several parameters therein Dr. Pendry provided theoretical proof that materials with a negative index of refraction allow for amplification of evanescent waves. Taking advantage of this idea he also proposed the idea of superlensing, using negative index materials to construct a lens capable of resolving images beyond the wavelength resolution limit that has plagued the scientific community from time immemorial [3].

In 1946 Dr. Edward Mills Purcell outlined a problem with Einstein's spontaneous emission probability equation. The rate as calculated was effective for an emitting particle in free space, but when the particle was contained within a cavity on the scale of the wavelength of the photon emitted the calculations were off, drastically. Dr. Purcell's solution was to introduce a multiplicative factor that would come to bear his name.

$$F_p = \frac{3Q\lambda^3}{4\pi^2 V} \tag{1.10}$$

The Purcell factor, in that it incorporates the Q or quality factor, is highly dependent on the resonance frequency of the particle. It is also a function of the volume of the cavity, and therefore the dimensions of the cavity. The Purcell effect has come to be shorthand for the impact of surrounding material boundaries on the emission of particle, like a cavity with only one wall [4].

One of the first experimentally verified instances of a negative index of refraction came in 2001 when Doctors Shelby, Smith, and Schultz realized the material that Smith and Shultz had proposed the year before along with Padila, Vier, and Nemat-Nasser [5,6]. Even that proposal was a reallocation of the negative permeability structure proposed by Pendry et al in 1999 and the negative permittivity structure set forth by Walter Rotman in 1962 to emulate the reaction of the ionosphere on signal propagation [7,8]. This composite material was constructed to achieve the desired results in the microwave range. This allowed for experimental confirmation of the feasibility of a metamaterial with negative refraction while keeping its components of reasonable scale such that they could be fabricated and manipulated with a minimum of specialized equipment. The unit cell of the material was composed of concentric split ring resonators imbedded in a fiberglass substrate oriented parallel to a series of thin metal rods. The concentric split rings with their combination of induced current and capacitance were responsible for the negative permeability while the array of rods contributed the negative permittivity [5].

The results of the experimental examination of this material were, as expected, highly dependent on polarization and frequency. The negative refraction of the structure being a function of concurrent resonances in the electric and magnetic field, the range of frequencies over which the negative permittivity and permeability expressed themselves was very limited.
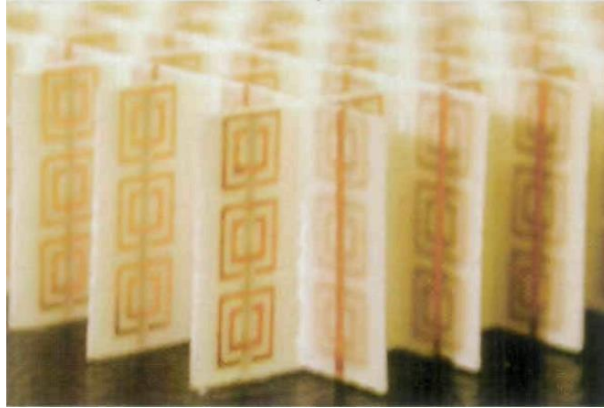
Fig. 1.3 Photograph of a negative refractive material that is active in the microwave range as presented by Shelby et al. Reproduced from Ref. [5].

While exploration of the microwave region was an important first step into the world of negative refraction, the necessity for the components to be on the subwavelength scale means that the methods used do not really translate well to other parts of the electromagnetic spectrum. Another impediment to using similar structuring to modify shorter wavelengths is that the resonant structures that allow for the coincident resonances on which negative refraction depends lead to high losses in the material as shown by Dr. Mark Ilich Stockman from Georgia State University [9]. To get around these unfortunate side effects and avoid unwieldy fabrication expense luminaries in the field started exploring the idea of anisotropic permittivities. By representing the dielectric permittivity of the material as a tensor the displacement field $\left(\vec{D} \right)$ need not be coincident with the electric field $\left(\vec{E} \right)$ which leads to the Poynting vector $\left(\vec{S} \right)$ and the wave vector $\left(\vec{k} \right)$ pointing in different directions. This is the core of negative refraction as laid out by Veselago.

There are several methods to go about this. In 2005 a collaboration between the (PI) University of New Mexico and Columbia University tackled this problem [10]. Their idea was to use a vertically stratified tri-layer structure consisting of a layer of gold, a layer of aluminum oxide, and another layer of gold with ovular holes in a repeating pattern. They differed the aspect ratio of the holes in different samples while leaving the spacing of the center of the holes constant. These holes were the source of the anisotropy in their system. This system was effective but only under the condition that the deposition of the strata that made up the system were extremely smooth and consistent. Using the methods of the time this was hard to achieve but it showed that anisotropy held promise as a pathway to negative refraction in infrared area of the spectrum.

An alternative procedure was realized by a collaborative effort between Princeton University and Oregon State University in 2007 [11]. To achieve the same general result they used alternating layers of doped semiconductors. They created a structure of ten alternating layers of $In_{0.53}Ga_{0.47}As$ and $Al_{0.48}In_{0.52}As$ stratified vertically. The use of uniform layers without the occlusions of the previous structure as well as materials that lent themselves to more consistent deposition procedures led to more consistent results.

The realization of projects like these harkened a new branch of metamaterial study, hyperbolic metamaterials. No longer was negative refraction solely limited to materials with both negative

permittivity and permeability. It had been shown that by manufacturing materials with a tensorial permittivity wherein only one of the spatial directions exhibited strong negative permittivity while the other two remained positive, negative refraction could be attained. This led to hyperbolic dispersion that is most easily visualized by looking at the shape of the isofrequency surface in k-space [12].
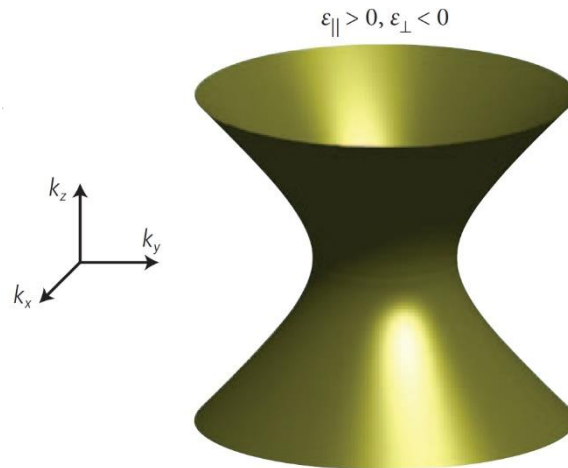

Fig. 1.4   Iso-frequency surface in k-space for a hyperbolic metamaterial
Reproduced from Ref. [12]

Here the permittivity of the structure is represented by the tensor

$$\varepsilon = \begin{bmatrix} \varepsilon_\parallel & 0 & 0 \\ 0 & \varepsilon_\parallel & 0 \\ 0 & 0 & \varepsilon_\perp \end{bmatrix} \tag{1.11}$$

As has been demonstrated in the previous examples this is most often achieved by the use of stratified media where the parameters of the constituent layers are used to define $\varepsilon_\parallel$ and $\varepsilon_\perp$ as

$$\varepsilon_\perp = \frac{\varepsilon_1 d_1 + \varepsilon_2 d_2}{d_1 + d_2}, \text{and } \varepsilon_\parallel^{-1} = \frac{d_1 \varepsilon_1^{-1} + d_2 \varepsilon_2^{-1}}{d_1 + d_2} \tag{1.12}$$

While these approximations may not hold over certain frequency ranges due to plasmonic effects and the like, they have been accepted in the community as standard so long as the scale of stratification remains significantly smaller than the vacuum wavelength of the incident radiation [12].

As the field of hyperbolic metamaterials has gained acceptance in the scientific community writ large it has come to be applied to more and more problems. These materials have been used extensively to study the enhancement of the emission of dipoles vis a vis the Purcell effect. They have also become instrumental to the search for superlenses in the last decade. Hyperbolic metamaterials have even been used as an experimental analogue for the Big Bang and the expansion of space-time that directly followed [13].

One of the applications of metamaterials that has piqued the interest of the general public the most is the advent of metamaterial cloaking. There are several different types of cloaking that are being pursued for different applications. Those that involve metamaterials will be where we focus our attention. The purest form of this cloaking is transformation-based cloaking. The idea behind this concept is that by modifying the permittivity and permeability of the material directly surrounding an object one can essentially transform the coordinate system of the space-time surrounding the object to be obscured such that the transmitted radiation, relative to the incident radiation, seems to pass through unencumbered. This form of cloaking is highly dependent on the angle of incidence, the geometry of the obscured object, and a very narrow frequency window [13]. The underlying ideas of this type of cloaking have been extended into another form of cloaking referred to as carpet cloaking. In this form of cloaking a discrepancy in the surface of a perfect conductor is obscured by a transformational layer of metamaterial much in the same manner as transformational cloaking. This form of cloaking however is concentrated on modifying scattered radiation rather than transmitted radiation [14]. The dependence on a backing of a perfect conductor would seem to preclude this method of cloaking from leading to the idealized cloaking that enters the mind of the general public when they think of the cloaking devices of science fiction and fantasy. However, pursuing these initial pathways of inquiry are the only way we will ever attain the idealized cloaking that has been portrayed by Hollywood for all these years.

My thesis is organized as follows. Presented in chapter one is a collaborative work between the theory group at Georgia Southern University and the experimental group at Norfolk State University. Dr. Durach and I provide a theoretical explanation of the experimental behavior of Eu^{3+} ions placed in close vicinity to metal films of different thickness. In this exploration, we utilize the dyadic Green's function approach to explain the unique behavior of the Eu^{3+} dipole transitions as a function of the thickness of the metal and the distance separating the dipoles from the metal. Of particular interest is the difference in the behavior of the electric dipole transition compared to that of the magnetic dipole transition. We used our explanation of this discrepancy to develop the idea of the "near-field event horizon," a quantifiable boundary beyond which all of the energy emanating from the dipole is utilized in the near-field, leaving nothing to escape into the far-field and thereby be picked up by experimental equipment.

Chapter two examines the optical properties of uniaxial metamaterials. The metamaterial considered here is a metal nanowire array. First, using the effective medium approximation we modelled the metasurface as a homogeneous, anisotropic slab. We showed that such a slab although being similar in form to a traditional wire-grid polarizer, surprisingly acts as a half wave plate with thicknesses as low as 30 nm and at larger thicknesses can exhibit quarter wave plate behavior. This characteristic is a consequence of very rapid phase difference accumulation caused by the simultaneous epsilon near pole (ENP) and the epsilon near zero (ENZ) response along different in-plane directions of the metasurface. Independently, this result was confirmed by calculations made by another GSU photonics theory group member Matthew LePain, who semi-analytically solved Maxwell's equations and directly computed the electromagnetic response of the metal nanowire array.

In chapter three, we propose a new class of optical resonators which we term metasurface cavities. We consider two types of those – Type I cavities are bounded by a metasurface and a conventional reflector and Type II are bounded by two uniaxial metasurfaces. Using the multi-mode transfer matrix approach which we developed to describe the photonic properties of the proposed structures, we show that the resonances that these cavities support are a hybridization of TM and TE polarized fields inside of the cavity and feature low-loss incident power redistribution over the output polarization channels, clover-leaf anisotropic dispersion, and other unique properties which are tunable and useful for multiple applications. We employ these ideas to predict, for the first time, the existence of novel photonic resonances namely hyperbolic Fabry-Pérot resonances and hyperbolic Tamm plasmons in metasurface cavities with homogeneous dielectric and distributed Bragg reflector (DBR) cores.

The material comprising this thesis was derived from papers published in which the candidate was the first listed author or the first listed author from Georgia Southern University.

Chapter 1: R. Hussain, **D. Keene**, N. Noginova, and M. Durach, "Spontaneous emission of electric and magnetic dipoles in the vicinity of thin and thick metal" Optics express, **22**, 7744-7755 (2014**)**

Chapter 2: **D. Keene**, M. LePain, and M. Durach, "Ultimately Thin Metasurface Wave Plates". Submitted for publication. Preprint at: arXiv preprint arXiv:1512.08139. (2015)

Chapter 3: **D. Keene** and M. Durach, "Hyperbolic resonances of metasurface cavities" Optics Express **23**, 18577-18588 (2015).

Chapter 2

Spontaneous emission of electric and magnetic dipoles
in the vicinity of thin and thick metal

Reproduced from the original article: R. Hussain, **D. Keene**, N. Noginova, and M. Durach, Optics express, **22**, 7744-7755 (2014)

The effects of the local environment on spontaneous emission are commonly discussed in terms of the Purcell effect [3] accounting for a modification of the photonic mode density and a subsequent alteration of the dipole emission rate [15-18]. Depending on the degree of modification of electric and magnetic components of optical modes, electric and magnetic dipoles can be affected in a different manner. This was discussed theoretically [17-21] and shown experimentally by observing changes in luminescence spectra of rare earth ions such as Eu^{3+} [22-31], having both magnetic and electric dipole transitions. It was suggested that Eu^{3+} ions can be used as a spectroscopic tool for probing the effect of optical magnetic resonance in plasmonic nanostructures [32], and for mapping local distributions of optical magnetic and electric fields in plasmonic metamaterials [21]. It was established that losses in nanostructured materials and changes in radiation patterns, which are different for magnetic and electric dipoles, are important factors for these applications [23-25].

Modification of electric and magnetic dipole emission associated with the presence of metal is an open problem in nano-optics and has recently attracted a lot of attention [25, 26]. If an emitter is placed in the vicinity of an ideal mirror and oriented parallel to the interface, one can expect a reduction of an electric and an enhancement of a magnetic dipole emission normal to the interface due to the boundary conditions for optical electric and magnetic fields [21, 30]. However, in very close vicinity to real metals at distances of about 30 nm, the opposite behavior has been recently observed: the emission of the electric dipole was enhanced while magnetic dipole emission was decreased near thin gold films and nano-strip arrays [23, 31].

The goal of the current work is to provide a better understanding of the effects of close vicinity of metal on electric and magnetic emitters. Here we restrict ourselves to planar geometry, considering dipoles very close to the surface of thin and thick metal films. The chapter is organized as follows. First, we describe an experiment where the distinctly different behavior of electric and magnetic emitters located near thin gold films was visualized in an optical microscope setup. Then, we provide a theoretical description where we show that that the contribution of Eu^{3+} emitters to far-field radiation demonstrates a threshold-like behavior dependent upon the distance between the emitters and the metal surface. In very close vicinity to the metal, all of the energy imparted on the emitter is required to establish a near field image within the metal, leaving nothing for radiation into the far field, which we refer to as being beyond the "near-field event horizon". Our model establishes a theoretical framework for the estimation of this threshold as a function of the thickness of the metal film. Also we show that it provides an adequate description of the effects observed in far field emission, which was originated from emitters located outside of this "event horizon."

Experiment

Highly luminescent Eu(TTA)$_3$(L18) chromophore material was synthesized in house, following Ref. [33]. The emission spectrum of Eu^{3+} has several well-distinguishable spectral lines, Fig. 2.1. The transition $^5D_0$ - $^7F_1$ with the emission at the wavelength, $\lambda = 590$ nm is associated primarily with a magnetic dipole [34] while the rest of the lines are primarily electric dipole transitions, including the strongest line, $^5D_0$ - $^7F_2$ with $\lambda = 611$ nm, originating at the same energy level.
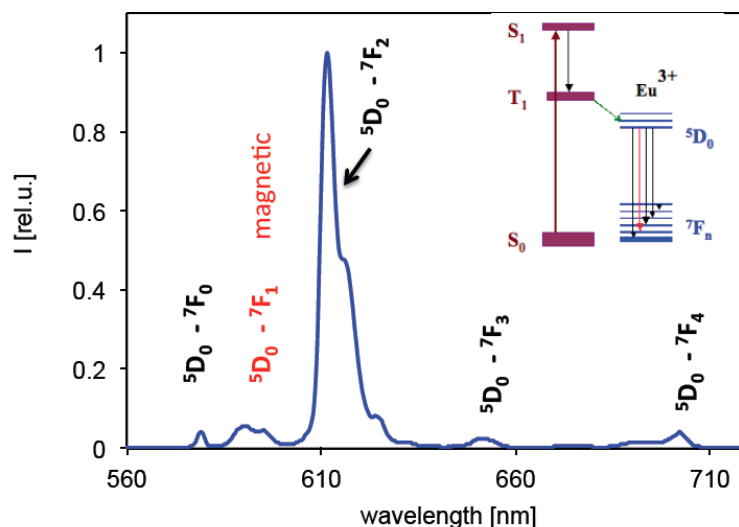

Fig. 2.1. Emission spectrum of Eu(TTA)$_3$(L18) amphiphilic complex. The excitation wavelength is 330 nm. Schematic of the levels is shown in insert.

The idea behind our experiment was to use the microscope setup where one could simultaneously observe the emission of Eu^{3+} placed in different surroundings: near thin metal, thick metal, and glass, which would be used as a reference. Then we would record and compare the effects of the different placement on the emission intensity separately for magnetic and electric transitions.

The substrates were fabricated with thermal deposition of gold or silver on a glass substrate through a standard STM mesh, 656-300-AU, purchased from *Ted Pella Inc*. Such a deposition produced 7 μm x 7 μm square patches of metal with 2 μm distances between each other, arranged in square blocks of ~50 x 50 μm size with 15 μm distances between blocks. The thickness of metal after the first step of deposition was ~ 50 nm as measured with the *Bruker DektakTX* profilometer. In order to obtain metal squares of two different thicknesses on the same substrate, we covered a half of the sample, and continued the thermal deposition. After the second phase, the thickness of squares at the exposed part was in the order of 170 nm.

Solutions of Eu(TTA)$_3$(L18) complex and polystyrene in chloroform were mixed in the proportion 1:5. 30-microliter drop of the mixture solution was spread on a water surface. After

evaporation of chloroform, a thin polymeric film was formed on the water surface. Such a process produced films with practically uniform thickness (which was confirmed with the profilometer after transferring the film to a flat surface). Immersing the substrate with metal squares, the film was transferred to the substrate covering both squares and a space between them. The thickness of the Eu^{3+} polymeric films was in the range of 30-40 nm.

The microscope images were recorded using *Zeiss Imager Z2m* microscope equipped with *Axiocam* camera. The luminescence of Eu^{3+} was excited with UV light at $\lambda = 325$ nm, which was brought to the sample with the optical fiber from the CW He-Cd laser. In order to record the emission signals at electric and magnetic transitions separately, interferometric filters for 610 nm and 590 nm correspondingly were inserted in the recording channel. The signal at 590 nm was relatively weak, that restricted us to use the 20x resolution objective of microscope.

The images obtained in the sample with thin gold are shown in Fig. 2.2. In Fig. 2.2 a, the golden squares seen in the standard reflection mode (using the microscope light source) correspond to square arrangements of small gold patches. The total emission, Fig. 2.2b, is brighter on the gold than on glass between them. However, the image clearly shows the presence of the luminescent film on both gold and glass.
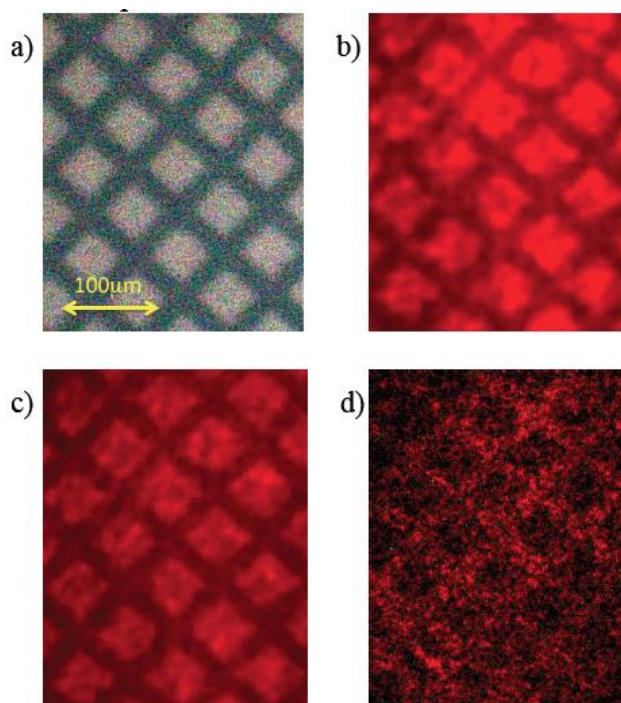

Fig. 2.2. a) A substrate with thin gold squares in a standard reflection mode; Eu^{3+} luminescence: b) total; c) at 610 nm; d) at 590 nm

Images taken at 610 nm (strong electric transition) and 590 nm (magnetic transition) are shown in Fig. 2.3(c) and Fig. 2.3(d) correspondingly. As one can see, the image recorded at the electric dipole transition (Fig. 2.3(c)) is similar to the image with the total emission (Fig. 2.3(b)), which can be expected taking into account that the transition at 610 nm contributes of ~ 70% to the total signal. For the magnetic dipole emission, the contrast between gold and glass is the opposite (Fig. 2.3(d)): the film on gold is darker than on glass interspacing.

Such a difference in contrasts for magnetic and electric dipole emission exists only if gold is thin (50 nm). At larger thicknesses of metal, both electric and magnetic dipoles show similar behavior. In order to clear demonstrate this, the polymeric film with Eu^{3+} was deposited onto a substrate having both thick and thin metal patches in such a way that the polymeric film of almost uniform thickness covered both thick and thin metal patches and bare glass.

In Fig. 2.3a, recorded in the standard reflection mode, different thicknesses of gold squares can be distinguished by different colors of squares. The light colored squares (indicated with a circle at the top of the figure) were thicker (d ≈170 nm) and dark colored squares (bottom circle) were thinner (d ≈50 nm), Fig. 2.3(a). The images recorded at 610 nm and 590 nm are shown in Fig. 2.4((b), (c)). Some variation in the emission from top to bottom is related to non-uniform illumination due to the position of the excitation source. However, the character of contrast between gold squares and glass in the inter-space is clearly seen.

The image recorded at the electric dipole transition (Fig. 2.3(b)) shows much stronger emission intensity from the Eu^{3+} placed on the top of gold squares than that on the glass (inter-square spacing). The character of contrast does not depend on the thickness of gold: gold brighter than glass is seen for both thin and thick patches.

Fig. 2.3 a) Thick and thin (as indicated with circles) patches of gold on glass in reflected light. b) and c) Eu^{3+} luminescence at 610 nm and 590 nm correspondingly

The magnetic transition (Fig. 2.3(c)) shows the negative contrast (gold is darker than glass) only for the thin gold (see the bottom circle). The contrast between thick gold and glass was similar to what was observed for the electric transition (gold is brighter than glass, see squares in the top circle).

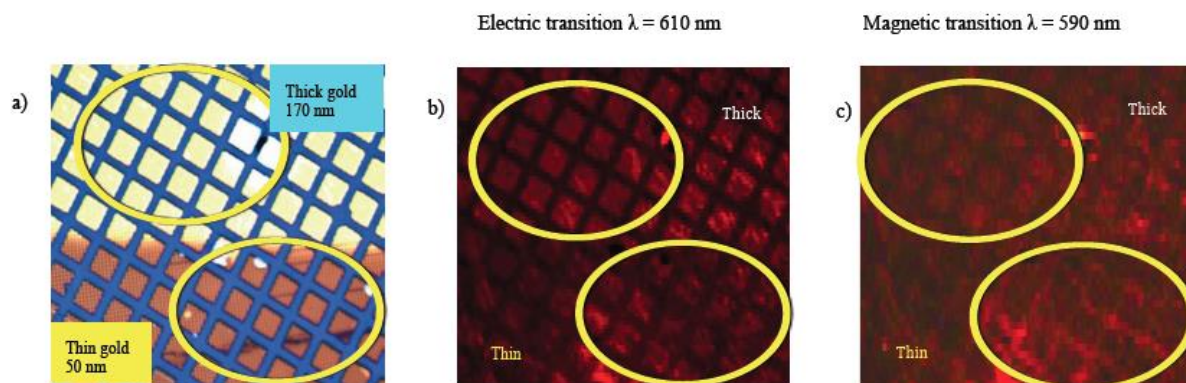Electric transition λ = 610 nm   Magnetic transition λ = 590 nm
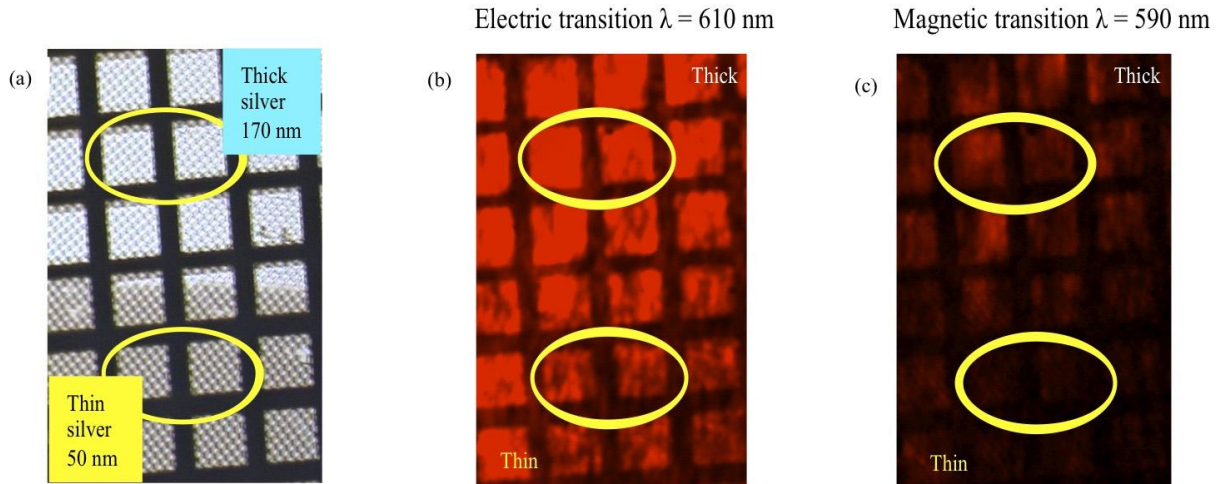
Fig. 2.4. a) Thick and thin (as indicated with circles) patches of silver on glass in reflected light. b) and c) Eu^{3+} luminescence at 610 nm and 590 nm correspondingly

We repeated the same experiment using a similar substrate having thin and thick silver patches, Fig. 2.4. In opposite to the observations with gold, the contrast was the same in all cases. For both electric and magnetic transitions, thick and thin silver squares looked brighter than glass, however, the magnetic dipole emission was significantly weaker on the top of thin silver than that on thick silver.

Theory

Our formulation is based on the dyadic Green's function approach for layered media [35]. Consider the structure composed of a glass substrate with refraction index n_g, a metal film with thickness a and a polymer layer with thickness d and refraction index n_p, containing a dipole separated by distance h from the metal (see Fig. 2.5). We show that the behavior of the emitters is strikingly different depending on the parameter h.

Fig. 2.5 Schematic of the structure.

The experiments are performed at CW UV excitation, which implies a steady state condition $P_{uv} = P_e + P_m + P_{non-em}$ where the excitation power P_{uv} is equal to the power released by the ions in the form of electric dipole emission P_e at the transition ${}^5D_0$ - ${}^7F_2$, magnetic dipole emission P_m at the transition ${}^5D_0$ - ${}^7F_1$ as well as P_{non-em} released through other radiative and non-radiative channels.
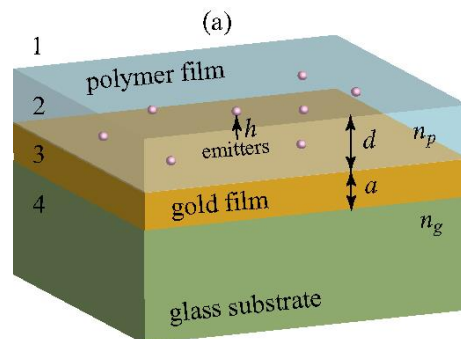
In this chapter we use normalized emission rates F_e and F_m defined through $P_e = \hbar\omega_e\Gamma_{0e}F_e$ and $P_m = \hbar\omega_m\Gamma_{0m}F_m$. Here the spontaneous emission rate for electric and magnetic dipoles in a homogeneous polymer medium are $\Gamma_{0e} = 4k_0^3|d_e|^2/(3\hbar n_p^2)$ and $\Gamma_{0m} = 4k_0^3|d_m|^2/(3\hbar)$. The normalized emission rates are equal to the integrals $F_e = \int_0^\infty \tilde{\rho}_e(k)dk$ and $F_m = \int_0^\infty \tilde{\rho}_m(k)dk$ over the density of states $\tilde{\rho}(k)$ per interval dk of the component k of the wave vector parallel to the layers of the structure. Note that the integrals not only include the density of states involving radiation of photons, but also the states involving near-field for $k > k_0$. Generic expressions for $\tilde{\rho}_e(k) \propto dP_e/dk$ and $\tilde{\rho}_m(k) \propto dP_m/dk$ are provided in the Supplementary Material (please see Eqs. (2.7) and (2.9)) and were derived following Ref. [35, 36].

In Fig.2.6 (a) we show the normalized relaxation rates F_e and F_m as functions of distance h from a metal film with thickness $a = 50$ nm. When emitters are placed next to the metal, the emission rate is strongly enhanced, especially for the electric dipole. Such modification of the dipole emission near an interface can be described in terms of the image model [17, 22-23]. In our case the dipoles are placed next to metal interface and the frequency range of the emission is close to the conditions of plasmon resonance of the metal, which leads to renormalized Coulomb interaction [37]. At the frequency of plasmon resonance, a source positioned within the near field zone at a distance h from the metal interface induces an image with the amplitude multiplied by a factor

$$\frac{\varepsilon_d - \varepsilon_m}{\varepsilon_d + \varepsilon_m} = \left(-1 + \frac{2i\varepsilon_m'}{\varepsilon_m''}\right) \approx \frac{2i\varepsilon_m'}{\varepsilon_m''}, \tag{2.1}$$

where ε_m' is the real part and ε_m'' is the imaginary part of the dielectric permittivity of the metal ε_m, such that $|\varepsilon_m'| \gg \varepsilon_m''$ and ε_d is the permittivity of the dielectric. This modified image formation can also be understood from the fact that Fresnel coefficient for such an interface in the near-field limit, i.e. at high longitudinal momenta, is $r_p(k_\parallel \to \infty) = 1 - 2i\varepsilon_m'/\varepsilon_m''$ (compare this to the near-field of the super-lens of Ref. [3]). The induced near-fields of the image are produced by plasmonic waves, which destructively interfere far from the dipole and constructively interfere to form the dipole image next to the position of the source dipole.

Formation of the electric dipole image and the dominant contribution of this relaxation channel can be confirmed by the fact that the normalized relaxation rate F_e is directly proportional to h^{-3} for $h < 10$ nm as can be seen from Fig. 2.6 (a). Interaction of the electric dipole with its image results in an increased relaxation rate as well as strong quenching of radiation from emitters positioned near metal films.

Interaction of the magnetic dipole with the near-field created by it is different from that of the electric dipole. The dependence of F_m on h approximately corresponds to $h^{-0.8}$, which first of all means that in the plane geometry there is no near-field image in the form of a magnetic dipole. The near-fields created by a magnetic dipole near plasmonic metal nanostructures is a very interesting problem of optical magnetism, which will be considered elsewhere.
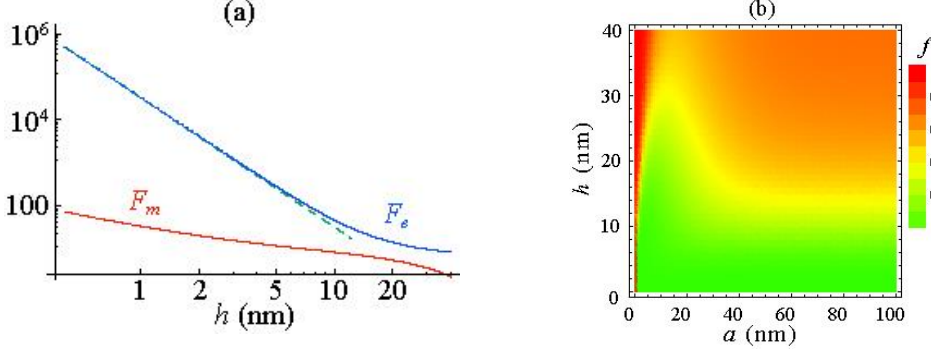

Fig. 2.6 (a) Normalized total emission rates F_e and F_m of electric and magnetic dipoles placed into a polymer film with $d = 40$ nm next to a gold film with $a = 50$ nm averaged over dipole orientation. (b) Factor f as a function of the metal film thickness and separation of emitter from the metal film h color coded as shown to the right of the graph. The graph is made for $d = 40$ nm, $\beta = 12$ and $\Gamma_{0e}/\Gamma_{0m} = 8$.

The intensity of radiation emitted by the dipoles toward the microscope at an angle θ to the normal of the structure per solid angle $d\Omega$ is given by

$$\frac{dI_e}{d\Omega} = \frac{P_{uv}}{P_e + P_m + P_{non-em}} \hbar\omega_e \Gamma_{0e} \rho_e(\theta) = \frac{P_{uv}\rho_e(\theta)}{F_e + (\Gamma_{0m}/\Gamma_{0e})F_m + \beta'} \tag{2.1}$$

$$\frac{dI_m}{d\Omega} = \frac{P_{uv}}{P_e + P_m + P_{non-em}} \hbar\omega_m \Gamma_{0m} \rho_m(\theta) = \frac{P_{uv}\rho_m(\theta)(\Gamma_{0m}/\Gamma_{0e})}{F_e + (\Gamma_{0m}/\Gamma_{0e})F_m + \beta'} \tag{2.2}$$

where it is assumed that $\omega_m \approx \omega_e$, and $\beta = P_{non-em}/(\hbar\omega_e\Gamma_{0e})$. Here $\rho(\theta)$ is the the local density of states involving emission of a photon in the interval of emission angles $d\theta$ normalized to the density of photons in the vacuum (see Supplementary Material). In our calculations below, we use $\Gamma_{0e}/\Gamma_{0m} \approx 8$ according to the estimations from the experiment (see Fig. 2.1). We use β as the only fitting parameter for our theory.

The numerators in Eqs. (2.1) and (2.2) correspond to the far field formation, while the denominators are responsible for the quenching. To illustrate how the quenching is included into our theory we introduce factor f, which represents the denominators in Eqs. (2.1) and (2.2). The physical meaning of f corresponds to the ratio between the full relaxation rate of emitters on glass to emitters on the metal films. We normalize f by the full relaxation rate on the glass substrate, since this rate is practically independent of h

$$f = \frac{(F_e + (\Gamma_{0m}/\Gamma_{0e})F_m + \beta)|_{a\to 0}}{(F_e + (\Gamma_{0m}/\Gamma_{0e})F_m + \beta)}.\tag{2.3}$$

The factor f is plotted in Fig. 2.6 (b). It can be seen that for emitters with $h < 10$ nm $f \approx 0$. This is due to strong quenching, which was described above. Quenching is also stronger for very thin metal films, where it is effective even for emitters separated by $h \approx 30$ nm from the metal. The divide between green and red areas in Fig. 2.6 (b) defines what we call the "near-field event horizon", beyond which emitters cannot radiate and be detected in the far field.

If an emitter is placed far enough from the metal the quenching is not as strong, which is represented by the factor $f \approx 1$. Those emitters contribute into far field emission and this emission can be explained based on the modified image model. Consider an emitter located next to air-metal interface right at plasmonic resonance. Reflection coefficients for high and low momenta are related as $r_p(k_\parallel \to \infty) = \frac{2r_p(k_\parallel=0)}{1+r_p^2(k_\parallel=0)}$ [38], with reflection coefficient at normal incidence for TM polarization being approximately equal to $r_p(k_\parallel = 0) \approx i$ (the exact equality is in absence of absorption). Thus, the reflection at normal and near normal incidence leads to appearance of phase-shifted image dipoles positioned in metal at distance h from its surface visible in the far-field and observed in the experiment with complex amplitudes

$$\boldsymbol{d}_i = -i\boldsymbol{d}_{0\parallel} + i\boldsymbol{d}_{0\perp},$$
$$\boldsymbol{m}_i = i\boldsymbol{m}_{0\parallel} - i\boldsymbol{m}_{0\perp},\tag{2.4}$$

where $\boldsymbol{d}$ and $\boldsymbol{m}$ are correspondingly electric and magnetic dipole moments and subscripts $\parallel$ and $\perp$ correspond to the parallel and perpendicular orientation vs the plane interface.

We explain the properties of the observed emission based on these images. The complex factors in front of the amplitudes lead to a lag in the oscillations of the images with respect to the original dipoles. The radiation emitted by the images travels toward the original dipoles and acquires the corresponding phase. At arrival to the position of the original dipole the emission constructively or destructively interferes with the emission from the original dipole. Since we observe the emission in the direction normal to the interface most of the emission comes from dipoles oriented parallel to the interface and this is where we will place our focus in the discussion.

The amplitude of the waves travelling toward our microscope from an electric dipole next to the metal-dielectric interface is given by

$$A = 1 - i \cdot \exp(2i\varphi_h),\tag{2.5}$$

where the phase $\varphi_h = k_0 n_p h$ is related to the propagation from the position of the image to the source. Note that emitters, whose radiation is not quenched, are separated from the metal by distance $h \approx 15 - 40$ nm, while the index of refraction for the polymer $n_p = 1.7$, which makes phase $\varphi_h \approx \pi/15 - \pi/4$. The combination of the quarter-period lag of the image dipole and the phase accumulated during the travel leads to the enhancement of the radiation from the electric dipoles positioned parallel to metal films. This in contrast with the image model based on an ideal reflector, but in agreement with the experimental data.

Now let us turn to the magnetic dipole emission. For a magnetic dipole on top of thick metal films enhancement is observed, while emission is decreased on top of thin films. If one reduces the thickness of the metal film to be on the order of the skin-depth l_s the reflection coefficient is changed to $r_p = i \tanh(a/l_s)$ and the far-field image described above is modified, so that its magnitude becomes reduced. Taking this into account the intensity of the magnetic dipole radiation normal to the structure is modified as

$$|1 + i \tanh(a/l_s) \exp(2i\varphi_h)|^2 \approx 1 + \tanh(a/l_s)^2 - 2\sin(2\varphi_h)\tanh(a/l_s).$$

It can be easily seen that, for example, for $\varphi_h \approx \pi/15$ this function represents enhancement for thick metal films $a \gg l_s$ and reduction of intensity for thin films $a \approx l_s$. It needs to be noted that the reflection characteristics of our actual structure (see Fig. 2.5) are more complex than the ones we use for the explanations we provide above, first of all, because the emission frequencies of Eu^{3+} transitions are somewhat detuned from the plasmonic resonance. Another factor is the additional reflections from the polymer-air and metal-glass substrate interfaces.

Now having established the groundwork for the theoretical description we turn to the exact situation with which we are presented experimentally. To find the intensities I_e and I_m measured by the microscope, we integrate Eqs. (2.1) and (2.2) over the radiative angle from 0 to θ_m corresponding to the numerical aperture of the microscope $NA = 0.5$. We also average the result over the position h of the emitters within the polymer films. We define the intensity contrast between emitters on metal films and emitters placed directly on the glass substrate as

$$\eta(a) = \frac{I_e(a)}{I_e(a=0)} - 1 \text{ and } \mu(a) = \frac{I_m(a)}{I_m(a=0)} - 1. \tag{2.6}$$

With this definition a positive value of contrast means that the signal coming from the emitters placed on gold films is stronger than the signal coming from those on the glass substrate. Negative contrast signifies the opposite situation.

The contrast ratios η and μ are shown as functions of the metal film thickness a for gold and silver in Fig. 2.7. The contrast η is positive for gold films thicker than $a \approx 20$ nm and is higher for thicker films, which agrees with the experimental results.
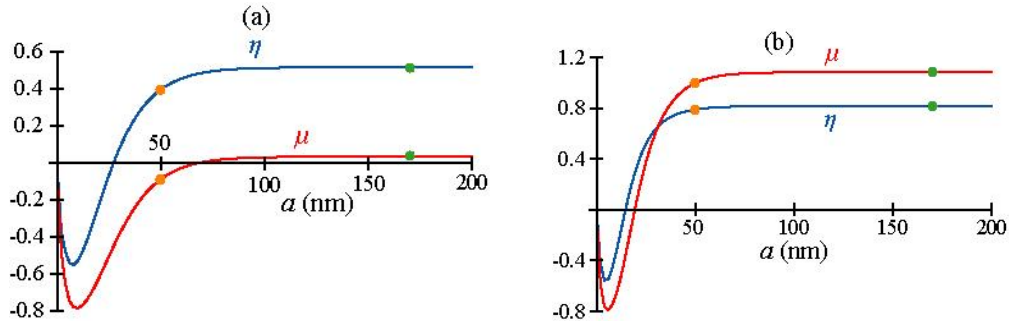

Fig. 2.7 (a) The contrast ratios η and μ (see Eq. (2.6)) for electric and magnetic transitions for gold film as a function of film thickness. (b) The same for silver film.

One can also see that the contrast ratio μ is negative for thin gold films with $a \leq 70$ nm and is positive for thicker films. We have placed orange and green dots in Fig. 2.7 to highlight the theoretical values corresponding to metal thickness, $a = 50$ nm and $a = 170$ nm, at which the experiments were conducted. It can be easily seen from Fig. 2.3 (b) and (c) that these contrast ratios correspond nicely to the experimental values. At the same time both η and μ are positive for silver films thicker than 20 nm in accordance with the experiments shown in Fig. 2.4 (b) and (c). It is through varying the fitting parameter β that we establish a curve for the function μ shown in Fig. 2.7 (a) that fits the experimental data for gold (Fig. 2.3 (c)), therefore locking down the value for $\beta = 12$, which seems to be reasonable for our highly luminescent material. Such sensitivity of magnetic dipole radiation to changes in the optical nanoscale environment can serve as yet another proof of the importance of investigations into the field of optical magnetism.

Conclusion

In conclusion, we have studied the effects of close vicinity to metal on spontaneous emission of electric and magnetic dipole sources through an optical microscope setup. Distinctly different behavior of electric and magnetic dipoles was demonstrated near gold films of a nanoscale thickness. We described the results theoretically based on the dyadic Green's function approach for layered media and proposed an interpretation based on modified image models for the near and far-field.

These results can find applications in probing and mapping of optical field distributions in plasmonic systems by spectroscopic methods.

Supplementary Material for Chapter 1

The electric local density of states $\tilde{\rho}_e(k)$ per interval dk of the component k of the wave vector parallel to the layers of the structure can be found to be

$$\tilde{\rho}_e(k) = \frac{1}{\hbar \omega_e \Gamma_{0e}} \frac{dP_e}{dk}, \tag{2.7}$$

where $P_e = ck_0/2 \cdot \text{Im}(\boldsymbol{d}_e^* \hat{G}_e(\boldsymbol{r}_0, \boldsymbol{r}_0) \boldsymbol{d}_e)$, and $\hat{G}$ is the electric dyadic Green's function at the position of the emitter $\boldsymbol{r}_0$. Using the Fourier representation of the Green's function we find

$$\frac{dP_e}{dk} = \frac{ck_0}{2n_p^2} \cdot \text{Re}\left[\frac{k}{k_z}\left(d_{e\parallel}^2 \cdot \frac{k_0^2 n_p^2}{2}\frac{\left(1 + r_{1s}e^{2ik_z(d-h)}\right)\left(1 + r_{2s}e^{2ik_zh}\right)}{1 - r_{1s}r_{2s}e^{2ik_zd}} + d_{e\parallel}^2\right.\right.$$
$$\cdot \frac{k_z^2}{2}\frac{\left(1 - r_{1p}e^{2ik_z(d-h)}\right)\left(1 - r_{2p}e^{2ik_zh}\right)}{1 - r_{1p}r_{2p}e^{2ik_zd}} + d_{e\perp}^2 \tag{2.8}$$
$$\left.\left.\cdot k^2 \frac{\left(1 + r_{1p}e^{2ik_z(d-h)}\right)\left(1 + r_{2p}e^{2ik_zh}\right)}{1 - r_{1p}r_{2p}e^{2ik_zd}}\right)\right].$$

Here $k_z = \sqrt{k_0^2 n_p^2 - k^2}$, r_{1p} and r_{1s} are reflection coefficients from the polymer-air interface for TM and TE polarized radiation, while r_{2p} and r_{2s} are corresponding reflection coefficients for reflection from the metal films.

The magnetic local density of states $\tilde{\rho}_m(k)$ can be found as

$$\tilde{\rho}_m(k) = \frac{1}{\hbar \omega_m \Gamma_{0m}} \frac{dP_m}{dk}, \tag{2.9}$$

where $P_m = ck_0 n_p^2/2 \cdot \text{Im}(\boldsymbol{d}_m^* \hat{G}_m(\boldsymbol{r}_0, \boldsymbol{r}_0) \boldsymbol{d}_m)$, and $\hat{G}$ is the magnetic dyadic Green's function. Finally, we find that

$$
\begin{aligned}
\frac{dP_m}{dk} = \frac{ck_0}{2} \cdot \text{Re} \Bigg[& \frac{k}{k_z} \left(d_{m\parallel}^2 \cdot \frac{k_0^2 n_p^2}{2} \frac{\left(1 + r_{1p} e^{2ik_z(d-h)}\right)\left(1 + r_{2p} e^{2ik_z h}\right)}{1 - r_{1p} r_{2p} e^{2ik_z d}} + d_{m\parallel}^2 \right. \\
& \cdot \frac{k_z^2}{2} \frac{\left(1 - r_{1s} e^{2ik_z(d-h)}\right)\left(1 - r_{2s} e^{2ik_z h}\right)}{1 - r_{1s} r_{2s} e^{2ik_z d}} + d_{m\perp}^2 \\
& \left. \cdot k^2 \frac{\left(1 + r_{1s} e^{2ik_z(d-h)}\right)\left(1 + r_{2s} e^{2ik_z h}\right)}{1 - r_{1s} r_{2s} e^{2ik_z d}} \right) \Bigg].
\end{aligned}
\tag{2.10}
$$

The intensity of radiation emitted into the air by the electric dipole with moment d_e and frequency $\omega = ck_0$ into a solid angle $d\Omega$ at angle θ to the normal in the far-field zone is

$$\frac{dI_e}{d\Omega} = \frac{c}{4\pi} \overline{|E(\theta)|^2} r^2 = \hbar \omega \Gamma_{0e} \rho_e(\theta). \tag{2.11}$$

Here $\overline{|E|^2}$ is the electric field at distance r from the sample averaged over the orientation of the dipoles. The spontaneous emission rate in a homogenous polymer medium is $\Gamma_{0e} = \frac{4}{3\hbar n_p^2} k_0^3 |d_e|^2$ and the local density of states involving emission of a photon into the air in the interval of emission angles $d\theta$ normalized to the density of photons in the vacuum for the electric dipole is

$$\rho_e(\theta) = \frac{1}{16\pi} \frac{\cos^2 \theta}{(n_p^2 - \sin^2 \theta)} \left(|t_{s+}|^2 + |t_{p+}|^2 \sin^2 \theta + |t_{p-}|^2 (n_p^2 - \sin^2 \theta) \right). \tag{2.12}$$

Similarly, the intensity of radiation by the magnetic dipole reads as

$$\frac{dI_m}{d\Omega} = \frac{c}{4\pi} \overline{|H(\theta)|^2} r^2 = \hbar \omega \Gamma_{0m} \rho_m(\theta). \tag{2.13}$$

Here the spontaneous emission rate for a magnetic dipole in a homogeneous polymer medium is $\Gamma_{0m} = \frac{4}{3\hbar} k_0^3 |d_m|^2$ and the normalized density of states for the magnetic dipole is

$$\rho_m(\theta) = \frac{1}{16\pi} \frac{\cos^2 \theta}{(n_p^2 - \sin^2 \theta)} \left(n_p^4 |t_{p+}|^2 + |t_{s+}|^2 \sin^2 \theta + |t_{s-}|^2 (n_p^2 - \sin^2 \theta) \right). \tag{2.14}$$

The amplitudes of the detected radiation $t_{p,s\pm}$ in Eqs. (2.11) - (2.14) are

$$t_{p,s\pm} = \frac{t_{21} \exp(i\varphi_{d-h}) \left[1 \pm R(a) \exp(2i\varphi_h)\right]}{1 + r_{12} R(a) \exp(2i\varphi_d)}, \tag{2.15}$$

$$R(a) = \frac{r_{23} + r_{34} \exp(-\phi_m(a))}{1 + r_{23} r_{34} \exp(-\phi_m(a))}, \tag{2.16}$$

where phases are given by $\varphi_x = k_0 n_p x$, and $\phi_m(a) = 2k_0 \sqrt{-\varepsilon_m} a \approx 2a/l_s$. The skin-depth is equal to $l_s = \left(k_0 \mathrm{Re}\sqrt{-\varepsilon_m}\right)^{-1} \approx 25$ nm at optical frequencies. The subscripts in the Fresnel coefficients for p-polarization $r_{ij} = \frac{n_i - n_j}{n_i + n_j}$ and $t_{ij} = \frac{2n_j}{n_i + n_j}$ correspond to the notations given in Fig. 5, while the Airy coefficient $R(a)$ represents reflection from the metal film [40]. The coefficients $t_{p,s\pm}$ contain all the information about the environment in which the emitters are located.

Chapter 3

Ultimately Thin Metasurface Wave Plates

Manipulation over polarization of light is one of the major applications of both macroscopic and nanoscopic optical components. The typical working principle of optical wave plates is based on the anisotropic optical response of birefringent media, in which polarization components are separated and accumulate a phase difference upon propagation. The main drawback of this approach is that the phase difference required to apply the needed polarization transformations is acquired over large distances due to low refraction index contrast, making the resulting wave-plate devices bulky [39]. The advance of metasurface photonics happening at the moment has already brought paradigm-changing ideas in the field of optics [40-42]. In particular, new ways to achieve polarization conversion were proposed, including metasurface cavities which allow for reduction of wave plate thickness to a fraction of a micron [43-47]. Several single metasurface structures were proposed as well, providing further reduction in size [48-51]. Nevertheless, the metasurface wave plates proposed to-date feature complex textures and require challenging fabrication. Two classical examples of metamaterials are parallel-plate and nanorod arrays and are known to exhibit strong anisotropy. Recently, it was experimentally shown that the anisotropic properties of epsilon-near-zero (ENZ) nanowire metamaterials lead to polarization rotation in 350-nm-thick metasurfaces based on Au nanorods [52]. The identical structure has been shown to exhibit effective Fabry-Perot (FP) resonances, whose frequencies are governed by effective medium parameters [53].

In this chapter we consider a metal nanowire grid metasurface, which can be considered as a monolayer of both parallel-plate array and nanowire array metamaterial (see Fig 3.1(a)). Two-dimensional wire grid arrays are known as the most commonly used and simplest types of *polarizers*. Here we demonstrate that, surprisingly, such metasurfaces with thickness of just 30-50 nm, despite their simple geometry and nanoscale dimensions, can in fact serve as an efficient *half- and quarter-wave plate* in the near-ir and visible range. This is achieved via interplay of simultaneous ENZ and epsilon-near-pole (ENP) response of these metasurfaces along different axes, allowing for rapid phase difference accumulation. Thicker 100-200 nm structures support a plethora of effective FP resonances for ordinary and extraordinary waves and provide a wide range of opportunities for polarization conversion. In particular, considering wire grid arrays proposed here with inhomogeneous lateral distribution of parameters such as metasurface thickness, metal fraction etc. may lead to a new generation of ultrathin polarization gratings, q-plates and other Pancharatnam-Berry phase optical elements [54-58], which currently attract a lot of attention in the photonics community. Interest in applying torque to nanoscale structures is emerging in such fields as biochemistry [59, 60]. In particular, quartz-based optical torque wrench devices are used [59]. Considering the plasmonic benefits inherent in noble metal nanostructures it would be extremely useful to be able to rotate them optically. The high mass density and the lack of natural anisotropy of noble metals complicate such rotations in comparison to quartz. The ultrathin highly anisotropic metal metasurfaces proposed in this chapter will bring such opto-mechanical manipulations into the realm of practicality.

Structure

Consider first a parallel-plate metal-dielectric array with period $d = d_m + d_d$, where $d_m = fd$ and $d_d = (1-f)d$ are the thicknesses of the metal and dielectric layers (Fig. 3.1 (a)). The dielectric permittivities are ε_m and $\varepsilon_d = n_d^2$ for the metal and dielectric and $f = d_m/d$ is the volumetric metal fraction. The dispersion of the photonic states is described by the Kronig-Penney equation. The photonic states with zero Bloch wave vector $k_x = 0$ can be separated into two symmetry classes for each polarization with dispersions $k_z(\omega)$ given by [61, 62]

$$p_m \tan\left(\frac{\alpha_m d_m}{2}\right) + p_d \tan\left(\frac{\alpha_d d_d}{2}\right) = 0 \ , p_d \tan\left(\frac{\alpha_m d_m}{2}\right) + p_m \tan\left(\frac{\alpha_d d_d}{2}\right) = 0 \qquad (3.17)$$
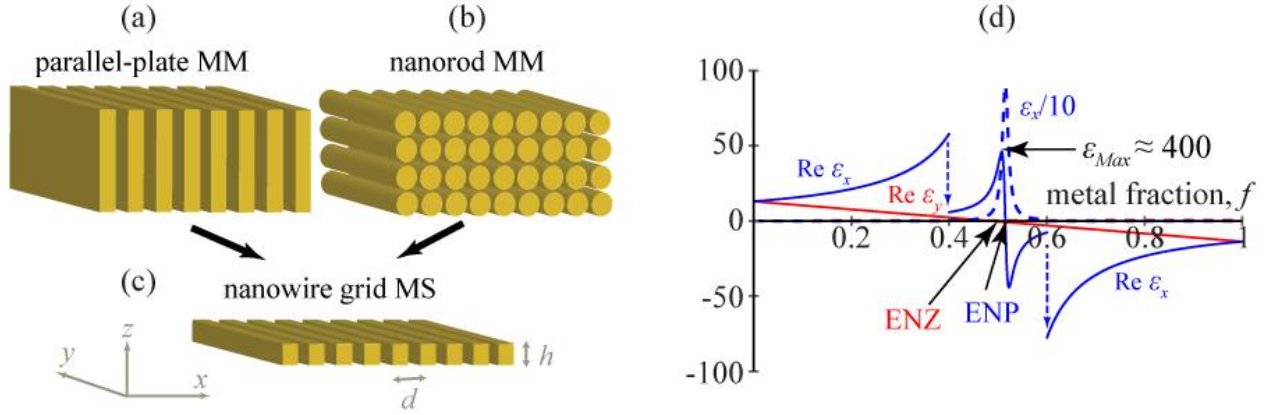

Fig. 3.1: Schematic of the structure and its typical dielectric response. (a), (b), (c) Correspondence between the parallel-plate and the nanorod metamaterials and the monolayer nanowire grid metasurface considered in this chapter. (d) Dielectric permittivities ε_x (blue for real and dashed blue for imaginary parts) and ε_y (red) as functions of metal fraction at $\hbar\omega = 2.2 \ eV$ for silver/GaAs metasurface, featuring ENP and ENZ.

where $\alpha_{m,d} = \sqrt{k_0^2 \varepsilon_{m,d} - k_z^2}$, $p_{m,d}^{TM} = \alpha_{m,d}/(k_0 \varepsilon_{m,d})$ and $p_{m,d}^{TE} = -\alpha_{m,d}/k_0$ for TM and TE polarizations, with the free space wave vector $k_0 = 2\pi/\lambda_0$.

The dispersion Eqs. (3.17) have an infinite number of solutions. In a subwavelength array $k_0 d \ll 1$, only modes with $\alpha_{m,d} d_{m,d} \ll 1$ efficiently couple to external radiation incident normally upon the array. In this case, the tangent functions in Eqs. (3.17) can be substituted by their arguments. Only the first of Eqs. (3.17) leads to reasonable dispersion equations in this limit, which are given by $k_z^2 = k_0^2 \varepsilon_x$ for TM fields (electric field along x-axis in Fig. 3.1 (a), (c)) and $k_z^2 = k_0^2 \varepsilon_y$ for TE fields (electric field along y-axis). The effective dielectric permittivities are given by

$$\varepsilon_x^{-1} = \varepsilon_m^{-1} f + \varepsilon_d^{-1}(1-f), \varepsilon_y = \varepsilon_m f + \varepsilon_d(1-f). \qquad (3.18)$$

Hence in the subwavelength case the array forms a metamaterial, with 3 bright modes, whose fields follow the effective medium approximation and all the other photonic states are dark plasmonic modes. Using Maxwell-Garnett approximation, the effective dielectric permittivities for the

nanorod metamaterial (Fig. 3.1 (b)) can be derived giving the same expression as in Eq. (3.18) for ε_y and a qualitatively similar expression for ε_x, featuring ENP transition [64]. Below we use Eqs. (3.18) for our effective medium calculations and model given in Fig. 3.1 (a) and (c) for exact calculations, but the same ideas apply to the nanorod metamaterials or metasurfaces as well. Note that the structures we consider here are different in principle from the structures considered in [52, 53], where the optic axes were perpendicular to the plane of the metasurfaces and the dielectric response in the plane of the metasurface was isotropic, which required large angles of incidence to achieve polarization manipulation. In this chapter we consider structures with optic axes in the plane of the metasurfaces perpendicular to the incidence direction, and anisotropy of the dielectric properties *in the plane* of the metasurface is crucial for the effects we predict.

Metamaterial Approximation

With this in mind, we first model the monolayer metasurface (Fig. 3.1(c)) as a layer of metamaterial with anisotropic dielectric response. We use the anisotropic characteristic matrix method, described in our recent paper, where we introduced a concept of hyperbolic resonances in metasurface cavities [47]. Here we consider a single metasurface. The metasurface responds to TM polarized normal incidence with incidence plane oriented along the x axis ($\phi = 0°$) as an isotropic material with dielectric permittivity ε_x. In the case of $\phi = 90°$ the optical response is fully determined by ε_y. According to the Polarization Rotation Equations [47] the reflection and transmission coefficients for TM and TE polarizations, r_p^{ϕ}, t_p^{ϕ} and r_s^{ϕ}, t_s^{ϕ}, at arbitrary ϕ can be determined in terms of that for $\phi = 0°$ and $\phi = 90°$ as

$$r_p^{\phi} = r_p^{0°} \cos^2 \phi + r_p^{90°} \sin^2 \phi, \, t_p^{\phi} = t_p^{0°} \cos^2 \phi + t_p^{90°} \sin^2 \phi, \tag{3.19}$$
$$r_s^{\phi} = \left(r_p^{0°} - r_p^{90°}\right) \sin \phi \cos \phi, \, t_s^{\phi} = \left(t_p^{90°} - t_p^{0°}\right) \sin \phi \cos \phi.$$

Note that at normal incidence the dielectric properties along the z axis ($\varepsilon_z = \varepsilon_y$ for parallel plates and $\varepsilon_z = \varepsilon_x$ for nanorods) do not affect the response of the metasurface, which removes the principal difference between the nanorods and parallel-plates.

In a conventional wire grid polarizer metal should be considered a perfect conductor $\varepsilon_m \to i\infty$, resulting in $\varepsilon_y \to i\infty$ and $t_p^{90°} = 0$; then Eqs. (3.19) are reduced to equations describing a polarizer. The optical properties of plasmonic metals in the visible frequency range are strikingly different from those of perfect conductors and are determined by finite permittivities ε_m with negative real part Re $\varepsilon_m < 0$. Therefore the nanowire grid metasurface proposed in this chapter is not a polarizer. We demonstrate that it can behave as quarter- and half-wave plates.

Consider a purely dielectric slab with thickness h and metal fraction $f = 0$. Typically, such a slab is not transparent with the exception of the Fabry-Perot (FP) resonance frequencies, which are the same for any polarization at normal incidence. Adding metal into the structure as we propose (Fig. 3.1(a)-(c)) has the opposite effect on modes in different polarizations. For the photonic states with the electric field polarized along y axis ($\phi = 90°$), the effective dielectric permittivity ε_y is linearly reduced from positive ε_d to ε_m with negative real part, passing through the epsilon-near-zero (ENZ) transition at metal fraction (see the red curve in Fig. 3.1(d))

$$f = f_{ENZ}(\omega) = \frac{\varepsilon_d}{\varepsilon_d - \mathrm{Re}\varepsilon_m}. \tag{3.20}$$

Correspondingly, for $f < f_{ENZ}$ the effective wavelength of the *ordinary* waves $\lambda_0/\sqrt{\varepsilon_y}$ is increased as metal is added, culminating in a virtually constant field at ENZ.

For the states with extraordinary polarization ($\phi = 0°$), the effective dielectric permittivity ε_x exhibits a non-monotonous behavior, featuring the epsilon-near-pole (ENP) transition during which the effective medium transforms from dielectric phase into a metal, passing through a region of strong absorption for extraordinary waves. The ENP transition (see the blue curve in Fig. 3.1(d)) occurs at metal fraction

$$f = f_{ENP}(\omega) = \frac{\mathrm{Re}\varepsilon_m}{\mathrm{Re}\varepsilon_m - \varepsilon_d} = 1 - f_{ENZ}, \tag{3.21}$$

For $f < f_{ENP}$ the dielectric permittivity ε_x increases with the increase of f reaching the maximum real value of ε_{Max} (Fig. 3.1(c)). This leads to a decrease in the effective wavelength $\lambda_0/\sqrt{\varepsilon_x}$ of the *extraordinary* waves. Note that the values of ε_{Max} can be very high, for example, Re $\varepsilon_x \approx 400$ in Fig. 3.1(d). This is an artifact of the effective medium approximation, since for such values of $k_z/k_0 = \sqrt{\varepsilon_{Max}}$ the condition $\alpha_{m,d}d_{m,d} \ll 1$ is not satisfied. Nevertheless, as we show below by semi-analytical solution of Maxwell equations for the structure in Fig. 3.1 (a) or (c), this leads to moderate quantitative deviation with no qualitative modification of our results.

The FP resonance energies $\hbar\omega_o$ ($\phi = 90°$) for ordinary (o-FP$_n$) and $\hbar\omega_e$ ($\phi = 0°$) extraordinary modes (e-FP$_n$) depend on metal fraction f and thickness of the metasurface h as

$$\hbar\omega_{on} = \frac{\hbar c}{\sqrt{\varepsilon_y(\omega_{on}, f)}}\left(\frac{\pi n}{h}\right), \hbar\omega_{en} = \frac{\hbar c}{\sqrt{\varepsilon_x(\omega_{en}, f)}}\left(\frac{\pi n}{h}\right), n \text{ is an integer} \tag{3.22}$$

The conditions of the FP resonances given by Eq. (3.22) can be resolved for the metal fraction as

$$f_{on} = f_{ENZ}(1 - n^2\xi^2), f_{en} = f_{ENP}\left(1 - \frac{1}{n^2\xi^2}\right), \xi = \frac{\lambda_0}{2n_d h} \tag{3.23}$$

This means that o-FP$_n$ approach the ENZ transition for small n, with $n = 0$ corresponding to ENZ exactly, while e-FP$_n$ approach the ENP in the limit $n \to \infty$. We confirm this by calculations in the effective medium approximation first. Using a 4×4 characteristic matrix approach [48], we calculate the reflectivity of the metasurface, which is shown in Fig. 3.2. Note that for calculations in this chapter we use the dielectric permittivity of silver [64] and a dielectric with refractive index $n_d = \sqrt{\varepsilon_d} = 3.6$, which corresponds to GaAs.

For a pure dielectric $f = 0$ the reflection spectrum of the metasurface is composed of FP reflectivity dips separated by broad bands of strong reflection for both $\phi = 0°$ (Fig. 3.2 (a)) and at $\phi = 90°$ (Fig. 3.2 (b)). As metal is inserted e-FP$_n$ at $\phi = 0°$ and o-FP$_n$ at $\phi = 90°$ split and closely follow Eqs. (3.22)-(3.7) (outlined by the dashed lines in Fig. 3.2), confirming our predictions.
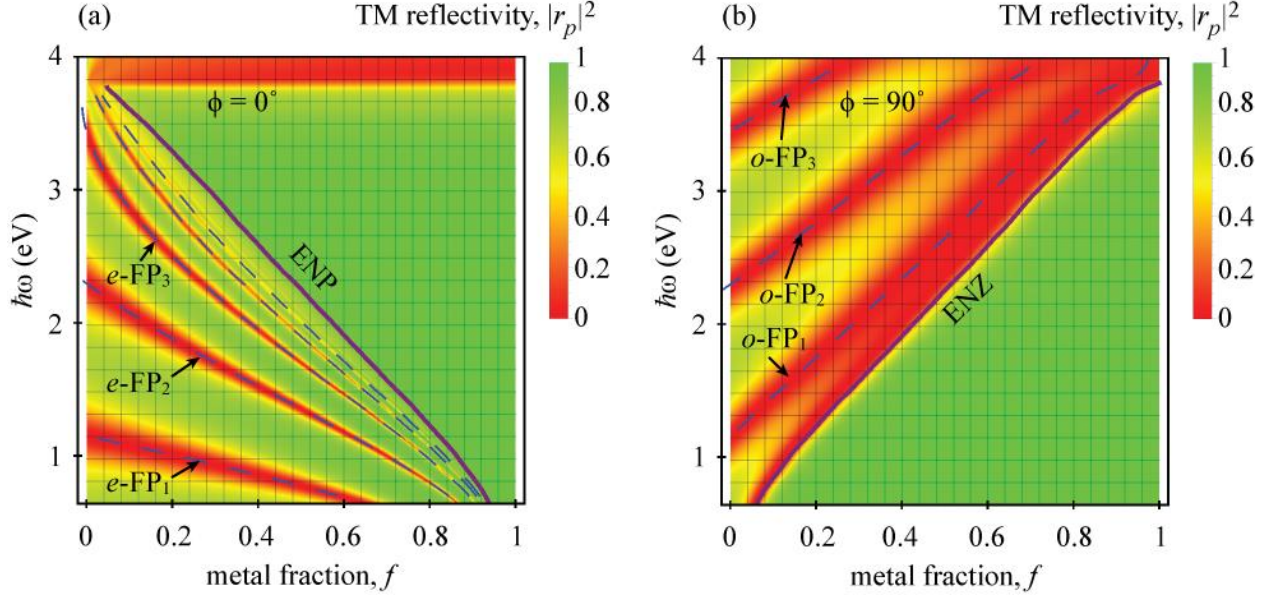
Fig. 3.2: Reflectivity of a 150-nm-thick metasurface as a function of the metal fraction f and energy of the incident radiation $\hbar\omega$ at (a) $\phi = 0°$ and (b) $\phi = 90°$ calculated using the effective medium approximation.

The energies of the FP resonances depend strongly on f, such that the nth extraordinary e-FP$_n$ mode may intersect mth ordinary o-FP$_m$ resonance if $n > m$ at energies which we denote as $E_{hw,mn}$, where "hw" stands for "half-wave plate" as will be explained below. Considering Eq. (3.19) for r_p^ϕ these intersections should explicitly appear at $\phi = 45°$. We plot the TM reflectivity $\left|r_p^{45°}\right|^2$ in Fig. 3.3 for metasurfaces with different thicknesses.

In Fig. 3.3(a) we plot reflectivity for a very thin metasurface with $h = 30$ nm. Since in this case $\xi \gg 1$ only one extraordinary e-FP$_1$ resonance with $f \approx f_{ENP}$ is visible. Higher order resonances are positioned closer to ENP and are extremely faint due to strong absorption in the effective medium at ENP. The only ordinary wave resonance present has $n = 0$ and corresponds to ENZ. The e-FP$_1$ and the ENZ intersect at $\hbar\omega = E_{hw,01}$ as indicated by the black dot. We show reflectivity for thicker metasurfaces $h = 100$ nm and 150 nm in Fig. 3.3 (b)-(c). As one can see the e-FP$_1$ shifts to lower energies and higher order extraordinary resonances become strong. Additionally ordinary resonances appear and intersect with higher order extraordinary resonances at $\hbar\omega = E_{hw,mn}$. The metal fractions f_{mn} at which these intersections occur can be found from the condition $f_{om} = f_{en}$ in the following form

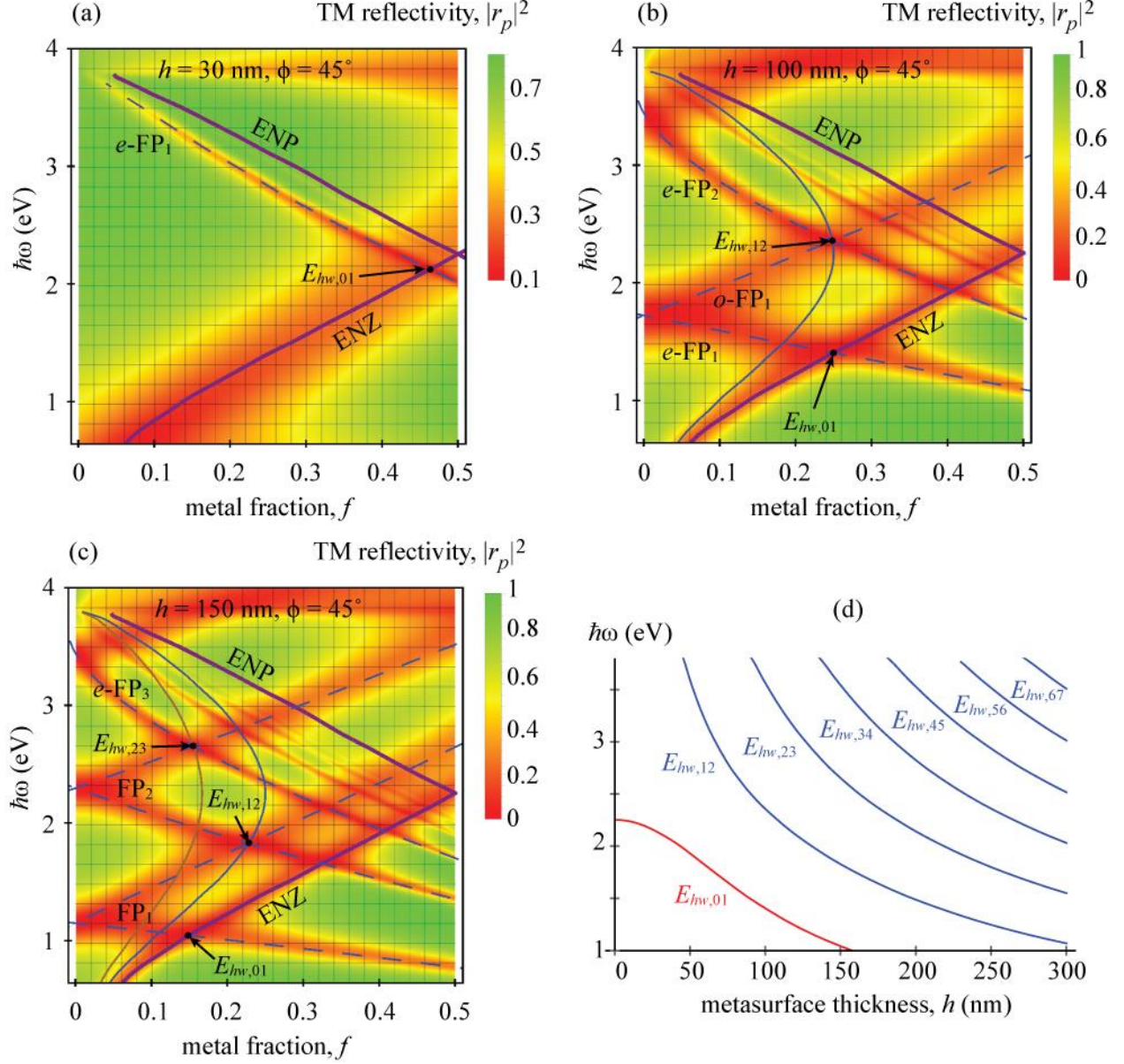$$f_{mn} = \frac{1 - n^2\xi^2}{1 - n^2\xi^2(2 - m^2\xi^2)} \qquad (3.24)$$

Fig. 3.3 Reflectivity of metasurfaces at $\phi = 45°$. (a) $h = 30\ nm$; (b) $h = 100\ nm$; (c) $h = 150\ nm$. (d) Dependence of the energies $E_{hw,nn+1}$ at which the metasurface is a half-wave plate on metasurface thickness.

We are mainly interested in intersections between the consecutive FP resonances at $E_{hw,nn+1}$. For very thin metasurfaces $\xi \gg 1$ the intersection between e-FP$_1$ and the ENZ occurs at $f_{01} \approx 0.5$ and with increase of the thickness h shifts down in energy along the ENZ line as shown in Figs. 3.3 (a)-(c). We plot the functions $f_{12}(\omega)$ and $f_{23}(\omega)$ in Fig. 3.3 (b)-(c) as blue and brown thin solid lines. The intersections $E_{hw,nn+1}$ are marked by black dots and as h is increased their energies are reduced, moving along the $f_{nn+1}(\omega)$ curves. This dependence of $E_{hw,nn+1}$ on metasurface thickness h is shown in Fig. 3.3(d). For thicker metasurfaces more FP resonances and their intersections appear in the plasmonic frequency range of silver ($\sim$1-4 eV).
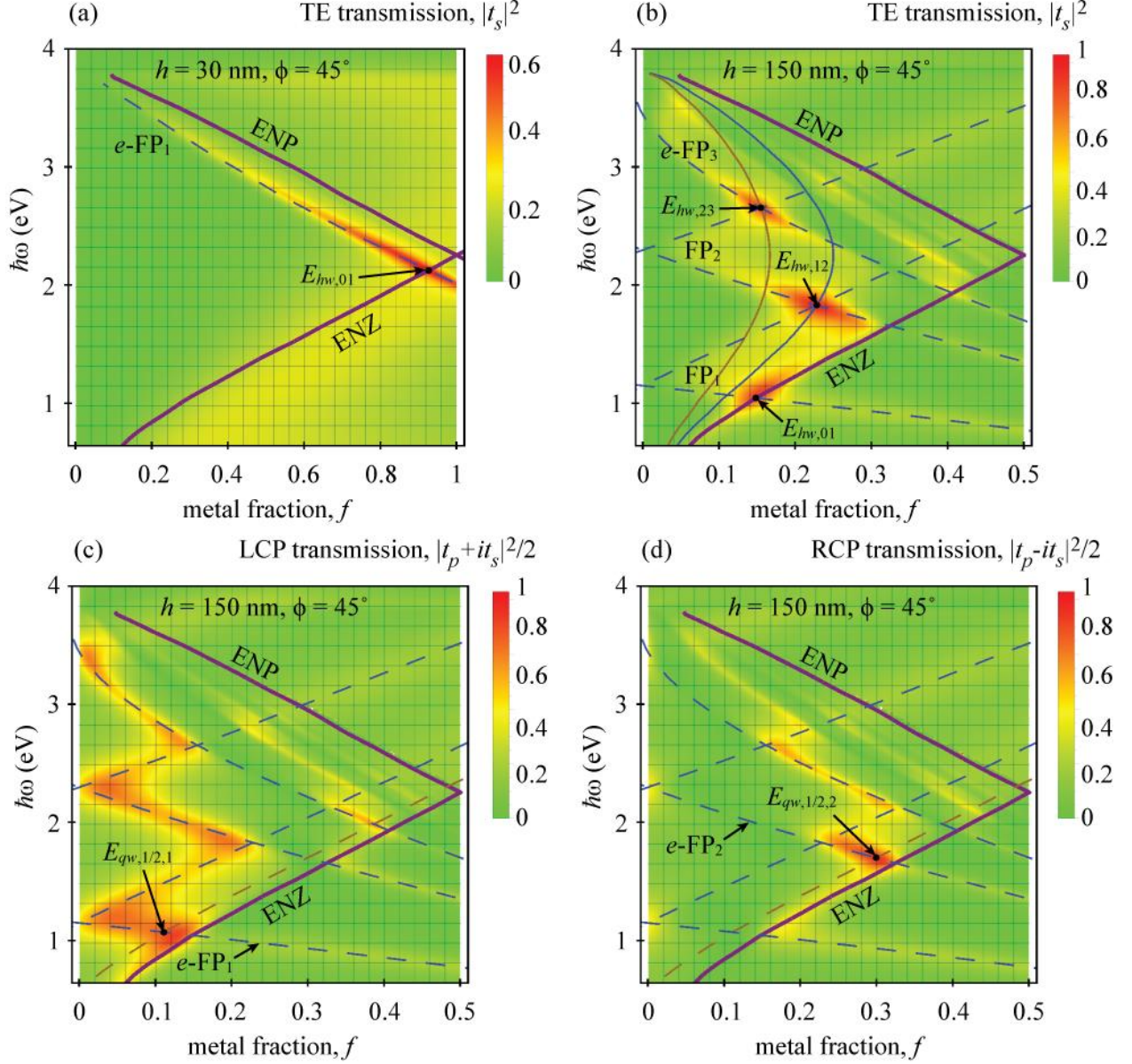
Fig. 3.4 (a), (b) TE transmission for $h = 30\ nm$ and $h = 150\ nm$ in response to TM polarized light. (c), (d) Transmission of left and right circular polarized light in response to TM polarized incidence for metasurface thickness $h = 150\ nm$.

The values of the transmission coefficients t_p for consecutive FP modes alternate in sign and are close to unity in magnitude. We can conclude from Eqs. (3.19) that at the intersections between o-FP$_n$ and e-FP$_{n+1}$ when the incidence plane is at angle $\phi = 45°$, the TM polarized incident radiation undergoes a 90-degree polarization rotation. Indeed, in this case $\left|t_p^{45°}\right|^2 \approx 0$ and $\left|t_s^{45°}\right|^2 \approx 1$. Similarly polarization rotation occurs when e-FP$_{n+1}$ intersect ENZ. In Fig. 3.4(a) we plot TE transmission $\left|t_s^{45°}\right|^2$ for $h = 30$ nm. Comparing this figure with Fig. 3.3(a) we confirm the polarization rotation with efficiency $\left|t_s^{45°}\right|^2 = 0.6$ at intersection of e-FP$_1$ and the ENZ at a remarkably thin metasurface. Note that loss of about 40% of the intensity of incident radiation is

due to high losses near the ENP transition (as seen in Fig. 3.1 (d)), since point $(f_{01}, E_{hw,01})$ is located next to ENZ-ENP intersection (see Fig. 3.4 (a)).

The nature of polarization rotation in the ENZ-ENP structure (Figs. 3.3(a) and 3.4(a)) which we propose here is easy to understand. The electric field of the ENZ ordinary wave directed along the y-axis (see schematics in Fig. 3.1 (a)-(c)) exhibits no phase change, while the extraordinary fields directed along the x-axis oscillate with wavelength $\lambda_x = \lambda_0/\sqrt{\varepsilon_{Max}} = 2h$, providing the required phase difference for the wave-plate effect in an extremely thin metasurface. We call this structure an *ultrathin ENZ-ENP wave plate*.

A larger thickness $h = 150$ nm metasurface (Fig. 3.4 (b)) has intersections at $\hbar\omega = E_{hw,nn+1}$ that lead to peaks with $\left|t_s^{45°}\right|^2 > 0.95$ in TE transmission. Hence we observe a half-wave plate behavior in a 150-nm-thick metasurface with close-to-100% efficiency. Further investigating this structure, we can find conditions in which the difference in phase shifts for ordinary and extraordinary waves lead to quarter-wave-plate behavior, converting linearly polarized incident radiation to circularly polarized transmission. This effect is strongest at intersections of $\hbar\omega_{o,1/2}$ and $\hbar\omega_{en}$ as can be seen in Fig. 3.4 (c)-(d). For $h = 150$ nm the efficient close-to-90% conversion into left-circular polarized (LCP) radiation happens at $E_{qw,1/2,1}$, while 90% conversion into right-circular polarized (RCP) occurs at $E_{qw,1/2,2}$. This high-efficiency conversion from linear to circular polarization indicates that the metasurfaces proposed here can acquire torques from the incident radiation with power $P_{inc} = $ mW of about $\tau \approx P_{inc}/\omega$ in the 10^3 pN · nm range, similar to the optical torque wrench structures previously proposed [59]. At the same time these metasurfaces have moments of inertia of comparable magnitudes, despite being composed of heavy Au atoms due to reduced dimensionality. This introduces the possibility of high-rpm rotation of plasmonic metal nanostructures.

Semi-analytical Solution

We confirm our results obtained using the effective medium approximation by solving Maxwell's equations semi-analytically for the nanostructure shown in Figs. 3.1 (a) and (c) using our recently developed numerical method [62]. To do so we first find the solution to the Kronig-Penney equation, which for normal incidence is given by Eqs. (3.17). As was noted before, if $\alpha_{m,d}d_{m,d} \ll 1$, these equations lead to the effective medium dispersion relations. The effective permittivity may become large at ENP, which leads to $k_z \approx \alpha_{m,d} \gg 1/d_m$, violating the applicability conditions for the effective medium approximation. We compare the exact solution of Eq. (3.17) for the bright extraordinary modes in the structure with period $d = 50$ nm with the effective medium dispersion, obtained using ε_x from Eq. (3.18) (see Fig. 3.1(d)). We are interested in deviations of the mode propagation wave vector k_z, since $k_z = n\pi/h$ is the condition for the extraordinary FP resonances.

We provide the three most extreme examples of such deviations for the two resonances: the e-FP$_1$ mode at $h = 30$ nm which requires $k_z = \pi/(30$ nm$)$ (shown as the right red dashed line in panels of Fig. 3.5) and the e-FP$_3$ mode at $h = 150$ nm requiring $k_z = 3\pi/(150$ nm$)$ (the left red dashed line in Fig. 3.5). The blue curves in Fig. 3.5 represent the exact solution of Eq. (3.17), while the green curves are the effective medium approximation. In Fig. 3.5(a) for $f = 0.3$ the exact solution intersects the $n\pi/h$ lines at lower frequencies than the effective medium approximation, as indicated by the blue and green arrows. The real part of the exact solution does not intersect the

$k_z = \pi/(30 \text{ nm})$ line, but comes close to it at $\hbar\omega = 2.33$ eV, so the resonance at this frequency should be expected.

In Fig. 3.5(b) for $f = 0.4$ we see that the exact dispersion coincides with the effective medium dispersion at $k_z = 3\pi/(150 \text{ nm})$. Meanwhile, for the exact dispersion at Re $k_z = \pi/(30 \text{ nm})$ two resonances exist within close proximity at $\hbar\omega = 2.1$ eV and $\hbar\omega = 2.2$ eV due to back-bending, instead of a single frequency for the effective medium at $\hbar\omega = 2.33$ eV. As can be seen from Fig. 3.5(c) the high-frequency root from the back-bending pair with Re $k_z = \pi/(30 \text{ nm})$ has much higher damping as it is overwhelmed by large Im k_z (represented by the dashed blue line), leaving only the low-frequency root as a resonance. It is important to note that this is always the case for the effective medium approximation regardless of f. For $f = 0.5$ the exact solution intersects the $n\pi/h$ lines at higher frequencies than the effective medium dispersion.
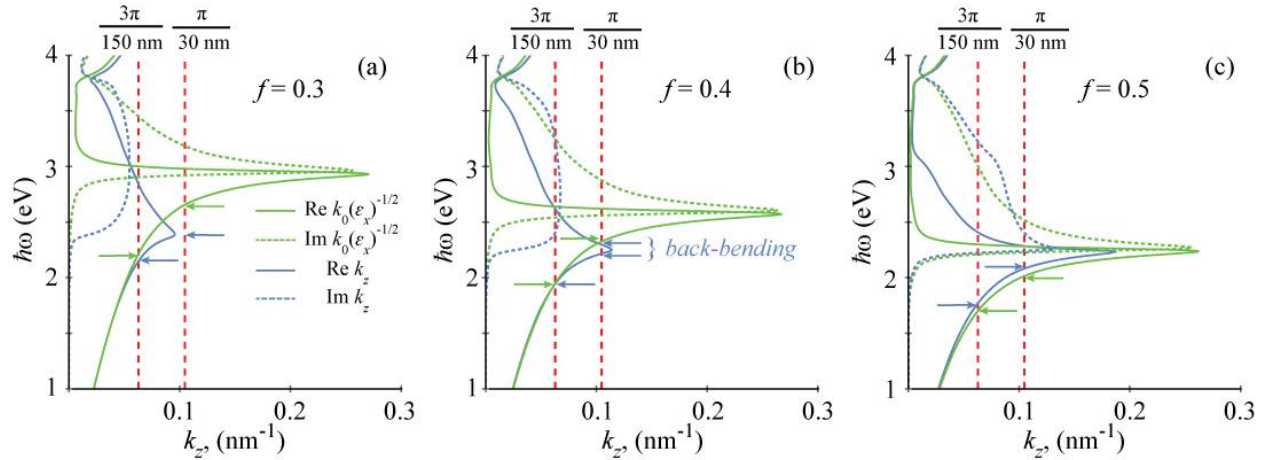

Fig. 3.5 Comparison of the exact solution $\omega(k_z)$ of Eq. (1) for period $d = 50 \text{ nm}$ and the effective medium approximation (the inverse function of $k_0\sqrt{\varepsilon_x(\omega)}$) with (a) $f = 0.3$; (b) $f = 0.4$; (c) $f = 0.5$.

This analysis directly translates into the optical response of the metasurface in the full solution of Maxwell's equations according to semi-classical method of Ref. [38] illustrated in Fig. 3.6. Panels (a) and (b) show the reflectivity of the structure at $h = 30$ nm and $h = 150$ nm respectively, which correspond directly to the effective medium calculations shown in Fig 3.3 (a) and (c). Similarly, panels (c) and (d) in Fig. 3.6 show TE transmittance in direct comparison to Fig. 3.4(a) and (b). The ramifications of the disparity between k_z calculated exactly and in the effective medium approximation near the ENP as outlined in Fig. 3.5 make themselves apparent in Fig.3.6 by the higher degree of curvature and back-bending in the energy as a function of metal fraction f for the e-FP$_1$ at $h = 30 \text{ nm}$ and e-FP$_3$ at $h = 150 \text{ nm}$ (Fig.2. 6 (a) and (b) respectively). This results in minor shifts in the parameters and insignificant changes in the magnitude for the half-wave (Fig. 3.6 (c) and (d)) and quarter-wave plate behavior (not shown) as manifested by the TE transmission at $\hbar\omega = E_{hw,nn+1}$.

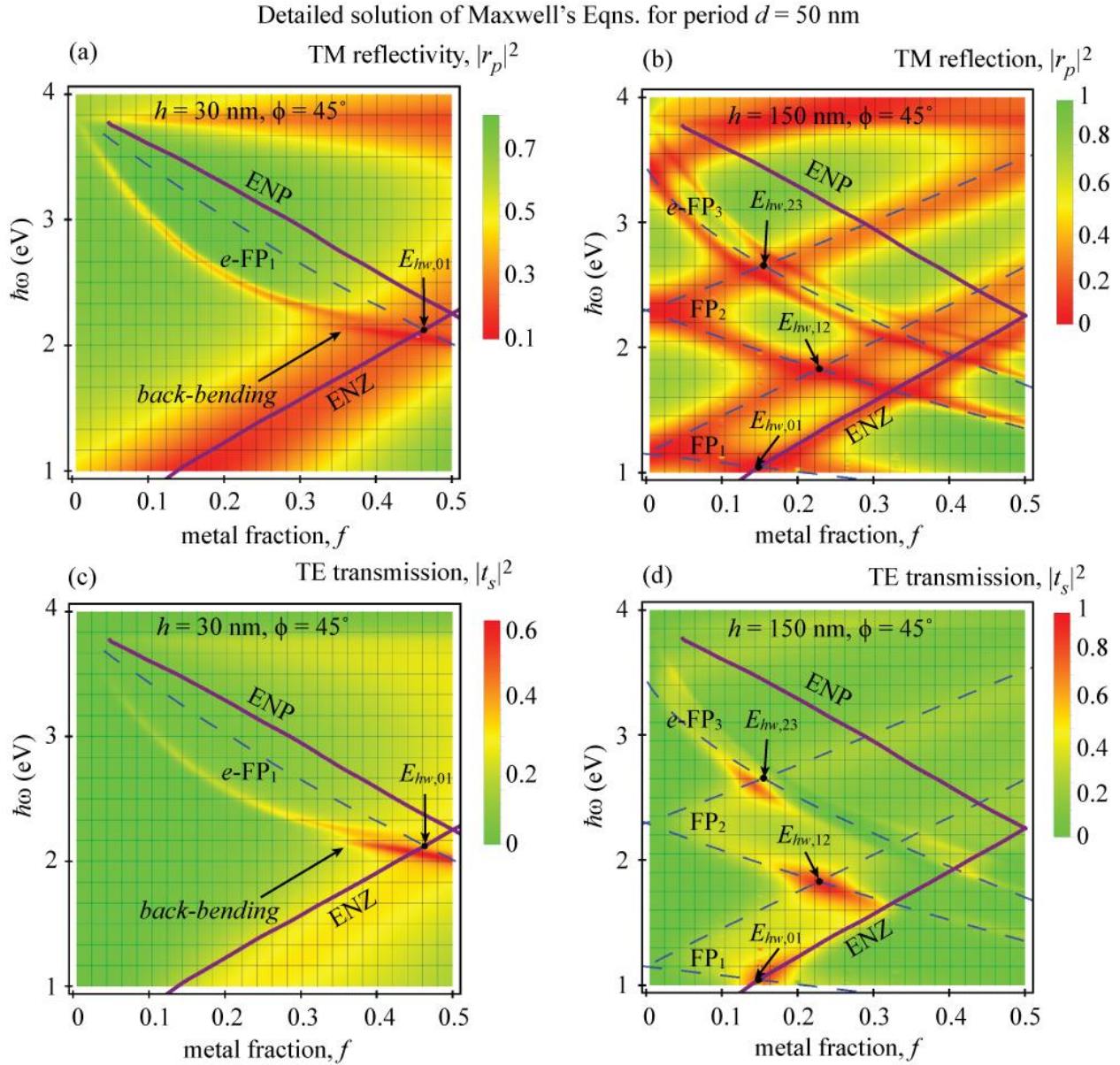Detailed solution of Maxwell's Eqns. for period $d = 50$ nm

Fig. 3.6 Optical properties on the metasurface shown in (Fig. 1(c)) according to the semi-analytical solution of Maxwell's equations. (a), (b) Reflectivity of the metasurface at $\phi = 45°$ for $h = 30\,nm$ and $h = 150\,nm$; (c), (d) TE transmission of the same metasurfaces.

Dispersion Relations

All the calculations shown before this point are for strictly normal incidence for the sake of simplicity as that is the most natural orientation for wave plates. We would like to demonstrate now that there is a range of incidence angles in which those properties persist. In Fig. 3.7 we show the 2-dimensional dispersion of the FP modes for $h = 150$ nm structure. For $f = 0.1$ (Fig. 3.7(a)) the two FP resonances shown (defined by $|r_p|^2 < 0.01$) do not intersect and feature highly anisotropic dispersion oriented along the respective axes. When these resonances intersect (Fig. 3.7(b)) they interfere to produce increased polarization rotation with 70% conversion efficiency in

the $\pm 10°$ range of angles around $\phi = 45°, 135°, 225°, 315°$ (see the red clover-leaf contour). In the other directions the structure is transmitting without polarization rotation as shown by the green contour. Note that all of the resonances exhibit an anisotropics parabolic dispersion.
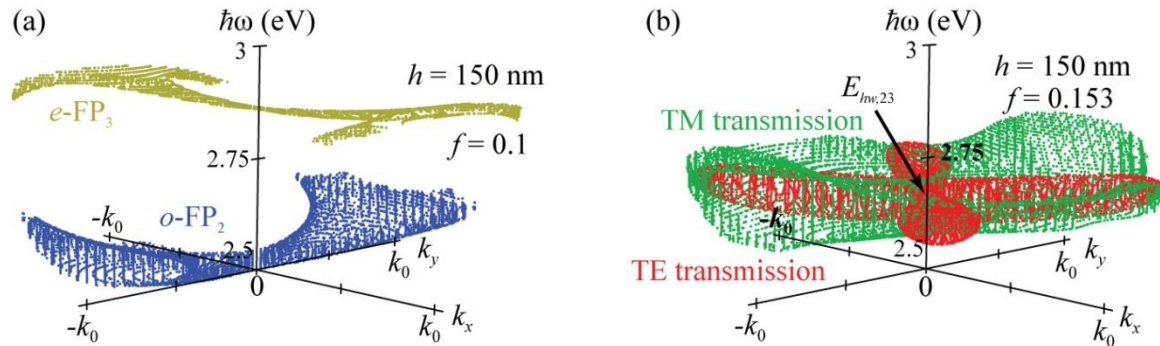
Fig. 3.7 Dispersion of the *e-FP*3 and *o-FP*2 resonances in $h = 150\ nm$ structure (a) off and (b) at the intersection $\hbar\omega = E_{hw,23}$.

Conclusion

In conclusion, we propose a nanowire grid metasurface, which can serve as an ultrathin ENZ-ENP wave plate as is shown in the effective medium approximation and confirmed by semi-analytical solution of Maxwell's equations. Polarization manipulation accomplished on sub-50 nm distances predicted here opens new possibilities for the fields of photonics and nanoscopic opto-mechanics.

Chapter 4

Hyperbolic resonances of metasurface cavities

Planar optical cavities and resonators are an integral part of optoelectronic components, providing opportunities for control over field distribution, enhancement, and localization on the nano- and microscale. Novel types of optical resonances have always attracted attention of the photonics community. As an example, the recent theoretical proposal [65] and experimental realization [66] of Tamm plasmon (TP) polaritons has been a source for a magnitude of studies and novel devices, ranging from compact lasers [67] to exiton-polariton BEC vortex guns [68]. Simple TP resonances are formed on an interface between a metal and a DBR and are optical surface waves, but there is a range of coupled hybrid resonances of TP nature [69-72]. In particular, it has been recently demonstrated that TPs are related to Fabry-Perot (FP) resonances and continuously transform into them when a metal-DBR-metal (M-DBR-M) structure is modified into a metal-insulator-metal (MIM) structure via reduction of dielectric contrast in the DBR [72]. An important avenue in the research on TPs is consideration of TP formation on interfaces between DBRs and localized metal nanostructures [73].

Interesting examples of recently proposed optical cavity resonances include ones in which the cavity contains a hyperbolic metamaterial core [74] or a cavity formed between a metasurface and a reflector [75, 76]. Metamaterials, formed by optical systems which are structured on the subwavelength scale, have been one of the central topics in photonics. One of the common examples of metamaterials are one-dimensional metal-dielectric arrays, which exhibit a wide range of phenomena, including various optical phases [77]. Generally modeled as uniaxial anisotropic media, depending on signs of real parts of dielectric permittivities, the uniaxial metamaterials can behave as anisotropic dielectrics, hyperbolic materials, or anisotropic metals. With this range of optical properties comes a large variety of optical resonant responses supported by these metamaterial structures [78].

In this chapter we propose a new class of cavities formed by a thin uniaxial metamaterial film (a uniaxial metasurface) and a conventional reflecting surface (Type I) or by two uniaxial metasurfaces (Type II) and show that such *metasurface cavities* (or *metacavities*) support novel resonances, which feature unique polarization properties, field distributions and anisotropic dispersion.

Uniaxial Metasurfaces.

First, let us consider the general properties of structures containing uniaxial metasurfaces. In this chapter we model such metasurfaces as thin films with thickness h of an anisotropic uniaxial medium with a diagonal dielectric tensor, whose component along the optic axis is $\varepsilon_\parallel$ .and is $\varepsilon_\perp$ in the perpendicular directions. Representing each metasurface this way with the optic axis directed in the plane of the metasurface serves as an approximation for a metal-dielectric grating, whose stratification axis coincides with the optic axis of the metasurface. The dielectric permittivity of the metasurface is defined in terms of the grating as $\varepsilon_\parallel = \varepsilon_m f + \varepsilon_d(1 - f)$ and $\varepsilon_\perp^{-1} = \varepsilon_m^{-1} f + \varepsilon_d(1 - f)$, where ε_m is the permittivity of the metal and ε_d is the permittivity of the dielectric, while f is the volumetric metal fraction [39].

Characteristic Matrix Approach.

We use two coordinate systems interchangeably: one with the *x*-axis going along the optic axis and another with an *x'*-axis lying at the intersection of the incidence plane and the *xy*-plane. We denote the angle between the *x*- and *x'*-axes as φ. The tangential components of the electric and magnetic field vectors are continuous throughout the structure and at different locations in the structure are related through matrix equations of the form

$$
\begin{pmatrix} H_{y'}(z_0) \\ E_{x'}(z_0) \\ E_{y'}(z_0) \\ H_{x'}(z_0) \end{pmatrix} = \hat{M} \begin{pmatrix} H_{y'}(z) \\ E_{x'}(z) \\ E_{y'}(z) \\ H_{x'}(z) \end{pmatrix}
\tag{4.1}
$$

where field components are taken in the *x'*-*y'*-*z* coordinates.

For concreteness we consider transverse-magnetically (TM) polarized excitation. Due to the anisotropic response of the metasurface pure transverse-magnetically polarized incidence generally produces transverse-electrically (TE) polarized fields as well. The first two components of the vectors in Eq. (4.1) correspond to the TM fields, while the second pair is the TE fields. The equation which describes the reflection and transmission properties of the structure in this case can be written as

$$
\begin{pmatrix} 1 + r_p \\ p_{p0}(1 - r_p) \\ r_s \\ -p_{s0}r_s \end{pmatrix} = \hat{M} \begin{pmatrix} t_p \\ p_{ps}t_p \\ t_s \\ p_{ss}t_s \end{pmatrix}
\tag{4.2}
$$

where r_p, t_p and r_s, t_s are the reflection and transmission coefficients in TM and TE polarizations correspondingly, while $p_p = k_z / k_0 \varepsilon$ and $p_s = -k_z / k_0$ with extra indices 0 and *s* denoting the incidence medium and the substrate. The characteristic matrix of the structure $\hat{M}$ is a 4×4 matrix [79]. To construct $\hat{M}$ we use a modified characteristic matrix approach which takes into account the anisotropic nature of the structure and coupling between the TM and TE polarizations. The matrices for isotropic media are block matrices composed out of 2×2 characteristic matrices positioned along the main diagonal, with blocks of zeroes off the main diagonal, representing the absence of TM/TE coupling in isotropic materials. The structure of characteristic matrices of the metasurfaces is more complex and must contain these off-diagonal elements to account for the coupling of TM and TE fields in the metasurface layer. We provide the detailed description of those matrices in the Supplementary Information.

Polarization Rotator Equations.

To understand the optical response of the structures consider first an excitation with incidence plane oriented along the optic axis $(\phi = 0°)$. In this case the electric field is along the optic axis. It is determined by $\varepsilon_{\parallel}$, is independent of $\varepsilon_{\perp}$, and all the fields in the structure are TM polarized. Similarly, in response to a normal TM incidence with $\phi = 90°$ the electric field is TM polarized and is determined by $\varepsilon_{\perp}$, not $\varepsilon_{\parallel}$. As we show in the Supplementary Information, both the TM and

TE reflection and transmission coefficients at arbitrary angle ϕ can be expressed through the reflection and transmission coefficients of the TM polarized fields at $\phi = 0°$ and $\phi = 90°$ as

$$r_p^\phi = r_p^{0°} \cos^2 \phi + r_p^{90°} \sin^2 \phi \qquad t_p^\phi = t_p^{0°} \cos^2 \phi + \sin^2 \phi$$
$$r_s^\phi = \left(r_p^{0°} - r_p^{90°}\right) \sin \phi \cos \phi \qquad t_s^\phi = \left(t_p^{90°} - t_p^{0°}\right) \sin \phi \cos \phi \tag{4.3}$$

These results, which we call Polarization Rotator Equations, imply that if the reflection and transmission coefficients are different for $\phi = 0°$ and $\phi = 90°$, then for the case of the incidence plane being at an intermediate angle, there should be an admixture of TE polarized response to purely TM polarized incidence, i.e. partial 90° polarization rotation. This gives way to a new class of resonances which we predict in structures containing uniaxial metasurfaces.

Type I Metacavities.

Consider a layer of homogeneous material between a conventional reflective structure with reflection coefficients r_p^R and r_s^R in TM and TE polarizations and a uniaxial metasurface with reflection coefficients r_{pp}^L and r_{sp}^L in TM polarization in response to TM and TE incidence correspondingly and r_{ps}^L and r_{ss}^L in TE polarization (see Fig. 4.1(a)).
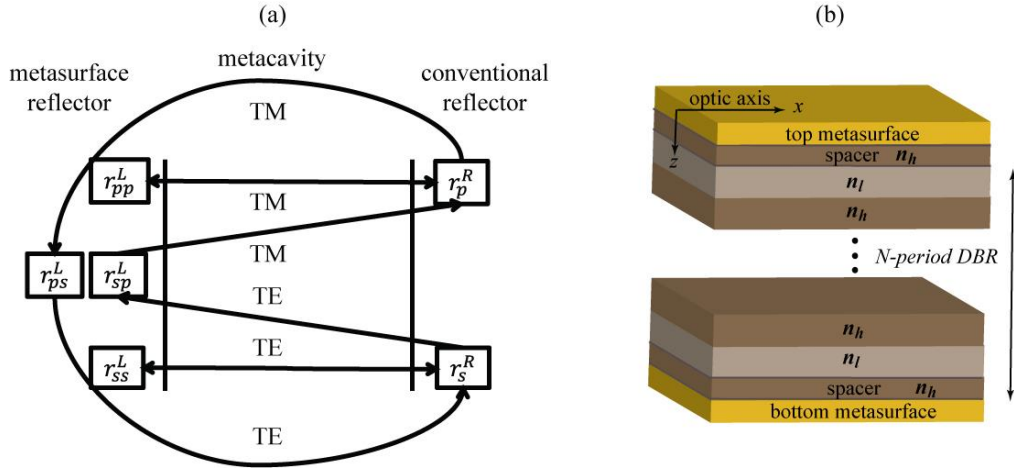
Fig. 4.1 Resonances of the metacavities. (a) Schematic of the resonances in Type I Metacavities (b) Schematic of the example structure, which is a Type I Metacavity at strong contrast in the DBR and a Type II Metacavity at no contrast.

In this case the resonance condition can be found from the following matrix equation

$$\begin{pmatrix} A_p \\ A_p r_{pp}^L + A_s r_{sp}^L \\ A_s \\ A_p r_{ps}^L + A_s r_{ss}^L \end{pmatrix} = \begin{pmatrix} e^{i\phi} & 0 & 0 & 0 \\ 0 & e^{-i\phi} & 0 & 0 \\ 0 & 0 & e^{i\phi} & 0 \\ 0 & 0 & 0 & e^{-i\phi} \end{pmatrix} \begin{pmatrix} B_p r_p^R \\ B_p \\ B_s r_s^R \\ B_s \end{pmatrix} \tag{4.4}$$

In Eq. (4.4) the first and third rows are the amplitudes of the wave propagating to the right in TM and TE polarizations correspondingly, while the second and the forth are amplitudes of the left propagating waves. The vector on the left-hand side is composed of the values of those amplitudes on the left boundary of the metacavity (metasurface), while the vector on the right is the amplitudes at the right side of the metacavity (conventional reflector). They are connected by a transfer matrix, where φ is the propagation phase inside of the cavity. Eq. (4.4) has nontrivial solutions only if

$$\left(r_{pp}^L + r_{ps}^L \frac{r_s^R r_{sp}^L e^{2i\phi}}{1 - r_{ss}^L r_s^R e^{2i\phi}}\right) r_p^R e^{2i\phi} - 1 = \left(r_{ss}^L + r_{sp}^L \frac{r_p^R r_{ps}^L e^{2i\phi}}{1 - r_{pp}^L r_p^R e^{2i\phi}}\right) r_s^R e^{2i\phi} - 1 = 0 \qquad (4.5)$$

This expression describes the resonances of a metacavity which includes a single uniaxial metasurface (Type I). It is different from the resonances of conventional cavities, described by $r^L r^R 2^{2i\phi} = 1$. These novel resonances involve co-propagation and multiple coupled reflections of TM and TE polarized waves as shown in Fig 4.1(a).

Hyperbolic Tamm Plasmons.

To give an example of such a resonance, we describe in detail the hyperbolic Tamm plasmons (HTPs), the existence of which we have recently predicted [80]. A schematic of the structure which supports HTPs is shown in Fig. 4.1(b). It is composed of two metasurfaces and a DBR. The metasurfaces and the DBR are separated by spacers with index of refraction n_h and thickness d_v. The $(LH)^N$ DBR array has Bragg frequency ω_B, with layers of a variable index of refraction n_l and a set index of refraction $n_h = 3.6$, such that $n_h > n_l$. This arrangement corresponds to GaAs/GaAlAs DBR.

The thicknesses of the corresponding layers are $d_l = \pi c/(2n_l\omega_B)$ and $d_h = \pi c/(2n_h\omega_B)$. The metasurfaces go through a variety of optical phases as the metal fraction f of the metasurfaces is changed, which is determined by the relationship between $\varepsilon_\parallel$ and $\varepsilon_\perp$. Decreasing the metal fraction f from 1 turns the metasurface first into an anisotropic metal, since both $Re[\varepsilon_\parallel]$ and $Re[\varepsilon_\perp]$ are negative. At intermediate values of f the metasurface behaves as a hyperbolic material with $Re[\varepsilon_\parallel] > 0$ and $Re[\varepsilon_\perp] < 0$. For small values of f the metasurface is a dielectric.

The HTP resonance is most expressed in the hyperbolic phase of the metasurfaces, when the DBR has such a strong contrast that the coupling between fields on different sides of the DBR is excluded. In such a situation the spacer between the hyperbolic metasurface and the DBR serves as a metacavity supporting HTP. The optical properties of such a *hyperbolic metacavity* are demonstrated in Fig. 4.2, where the dependences of the reflection spectra in TM and TE polarizations on metal fraction f are shown. The spectra feature a broadband stopgap for almost all plotted values of the parameters due to high contrast of the DBR ($n_h = 2.4$).
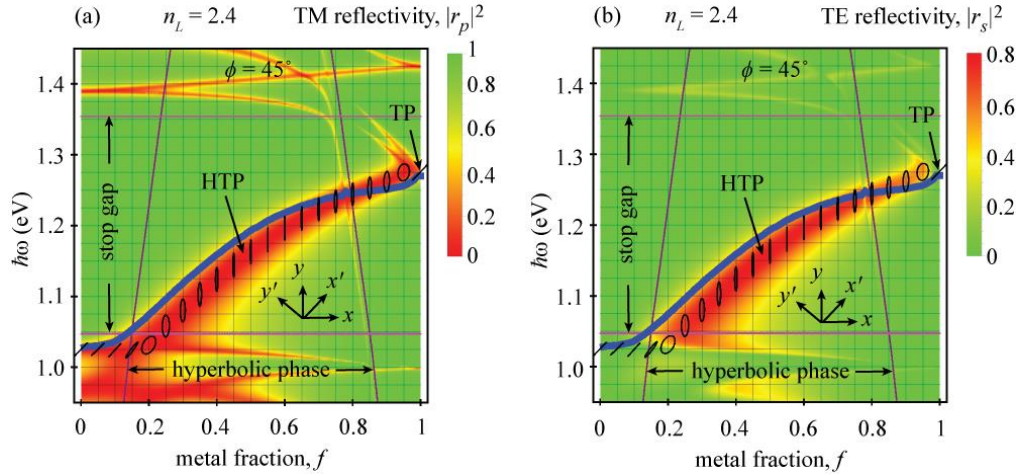
Fig. 4.2 Optical properties of the structure supporting HTPs. (a) TM reflectivity, $\left|r_p\right|^2$, as a function of excitation frequency $\hbar\omega$ and metal fraction f; (b) the same as (a), but for TE reflectivity, $\left|r_s\right|^2$.

The HTP is visible as a strong resonance in the center of the stopgap in Figs. 4.2. Note that the reflectance in Figs. 4.2 (a)-(b) is in response to normal incidence with $\phi = 45°$. For a metasurface in the isotropic metal limit ($f = 1$) HTP reverts to a simple Tamm plasmon (TP) with an isotropic reflection minimum. The conversion of a TP into an HTP is accompanied by a considerable reduction in the resonance frequency. As metasurfaces are modified from an anisotropic metal to an anisotropic dielectric through the hyperbolic phase one can observe a dramatic drop in the HTP frequency of about 0.25 eV. This is related to the HTP resonance transition from the top of the stop gap through the lower-energy bound of the stop gap where the DBR becomes transparent. This coincides with the transition of the HTP into the regime of the Fabry-Perot (FP) resonance.

In Figs. 4.2 (a)-(b) we plot polarization ellipses on top of the HTP resonance, which represent the electric field in the middle of the metasurface layer. The positioning of the centers of the ellipses corresponds to the minima of the resonance reflectivity $\left|r_p\right|^2$, while the orientation of the ellipses is plotted with respect to the spatial xy-axes (with xy-directions indicated in Fig. 4.2). At the TP limit ($f = 1$) the metasurface is just a thin metal film, an isotropic material, and the electric field polarization follows the direction of excitation at $\phi = 45°$. But as f is reduced, turning the metasurface into a hyperbolic material, the electric field inside of it is *pinned* to the y-direction perpendicular to the optic axis. In the hyperbolic phase the real part of the dielectric tensor component in the y-direction, $Re[\varepsilon_\perp] > 0$, while along the optic axis $Re[\varepsilon_\parallel] > 0$. Thus the pinning of the electric field in the hyperbolic phase corresponds to the metasurface polarizing along its metal-like axis.

The fact that the pinned electric field can be decomposed into TE and TM polarized fields (or x'- and y'-axes in the Fig. 4.2) shows that the response of the metasurface at the HTP resonance features a strong coupling between TM and TE polarizations. Both TM and TE polarized fields

are featured in the HTP mode and it is described quite well by the equation of the metacavity resonance Eq. (4.5). This is shown by the blue curves in Fig. 4.2 (see also Fig. 4.1(a)). Those blue curves are found as minima of the right-hand side of Eq. (4.5). This demonstrates that HTPs serve as a good example of Type I metacavity resonances.

The TM/TE coupling provides for an additional channel to distribute the incoming power. As shown in our previous work if $f = 1$ the incident power is mostly *absorbed* in the TP mode due to the trapping of optical fields, despite of the small modal fraction within the metal [72]. Coupling to the TE field results in re-distribution of the power from absorption into TE reflection as can be seen in Fig. 4.2(b) where TE reflectivity is shown to be around 80% of the incidence power at the HTP resonance.
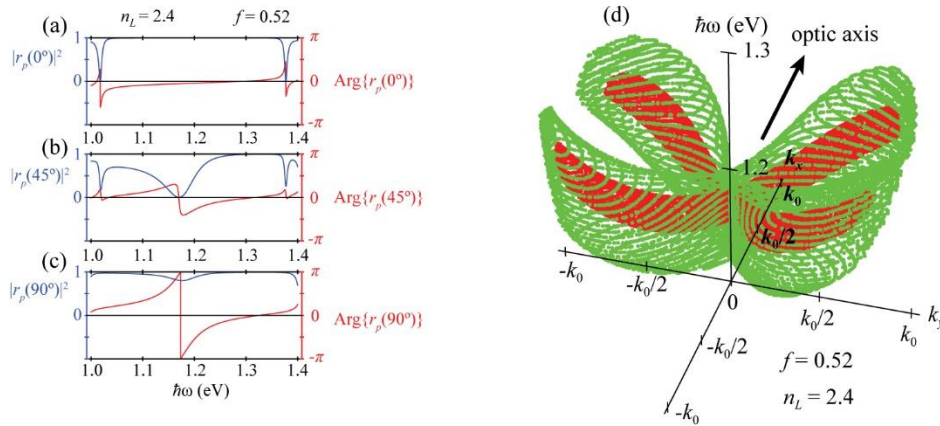

Fig. 4.3 Anisotropic nature of HTPs. (a)-(c) Formation of HTP resonance at $\phi = 45°$ due to difference of reflectivity at $\phi = 0°$ and $\phi = 90°$ in accordance with Polarization Rotation Equations (Eqs. (3)). (d) Clover-leaf parabolic dispersion of HTP modes.

The appearance of TE polarized fields in response to TM excitation can be further understood from the perspective of the Polarization Rotator Equations (Eqs. (4.3)). For incidence planes along and perpendicular to the optic axis the response is purely TM polarized, but it is different due to the difference between $\varepsilon_\parallel$ and $\varepsilon_\perp$. According to Eqs. (4.3) this leads to TE fields at intermediate angles ϕ, with the biggest magnitude of $|r_s|^2$ and a minimum of $|r_p|^2$ near $\phi = \pi/4$, where HTP resonance is the strongest. To demonstrate this, we show the spectra of TM reflectivities $|r_p|^2$ and $Arg\{r_p\}$ at $f = 0.52$ for $\phi = 0°, 45°, 90°$ in Figs. 4.3(a)-(c). At $\phi = 0°$ (Fig. 4.3(a)) the structure exhibits a strong reflectivity characteristic of the stop gap of the DBR, due to behavior of the metasurface as a dielectric with dielectric permittivity $\varepsilon_\parallel$ and $r_p(0°) \approx 1$. At $\phi = 90°$ (Fig. 4.3(c)) the metasurface acts as a metal in accordance with $Re[\varepsilon_\perp] < 0$. The reflection coefficient exhibits a weak TP resonance in the middle to the stop gap with $r_p(90°) \approx -0.9$. This leads to the full cancellation of

the TM polarized reflectivity at $\phi = 45°$ such that $r_p(45°) \approx 0$ at the HTP resonance according to Eqs. (4.3). Re-distribution of the reflected power into TE polarized reflection is observed as was pointed out above (see Fig. 4.2(b)).

In the hyperbolic phase the HTP mode is highly dependent on the angle of the incidence plane ϕ and is only present within $\approx 30°$ FWHM angular ranges centered around $\phi = \frac{\pi}{4} + \frac{\pi m}{2}$, where m is an integer. This is shown in Fig. 4.3(d) where the dispersion of HTP is shown. The presence of HTP can be judged by TM reflectivity being less than 50% within the green area and TE reflectivity being greater than 80% within the red-colored area. Thus HTPs feature a clover-leaf dispersion with highly anisotropic propagation properties. At other angles in the hyperbolic range the structure features a passive TM polarized 100% reflection.

We have previously demonstrated that TPs are related to Fabry-Perot (FP) resonances and continuously transform into them when a metal-DBR-metal (M-DBR-M) structure is modified into a metal-insulator-metal (MIM) structure via reduction of the dielectric contrast in the DBR [61]. It is interesting to see what happens to the HTPs when the same transformation is carried out. As can be seen from Fig 4.4(a), if the dielectric contrast in the DBR is reduced from $n_h/n_l = 3.6/2.4$ to 3.6/3.1 there is a profound splitting of the resonance into two modes – lower-energy symmetric HTP (s-HTP) and anti-symmetric HTP (a-HTP). The magnetic field in the TM component of the symmetric (anti-symmetric) mode is predominantly symmetric (anti-symmetric) upon reflection with respect to the center of the structure. The splitting is due to hybridization of the HTPs at different metal-DBR interfaces.
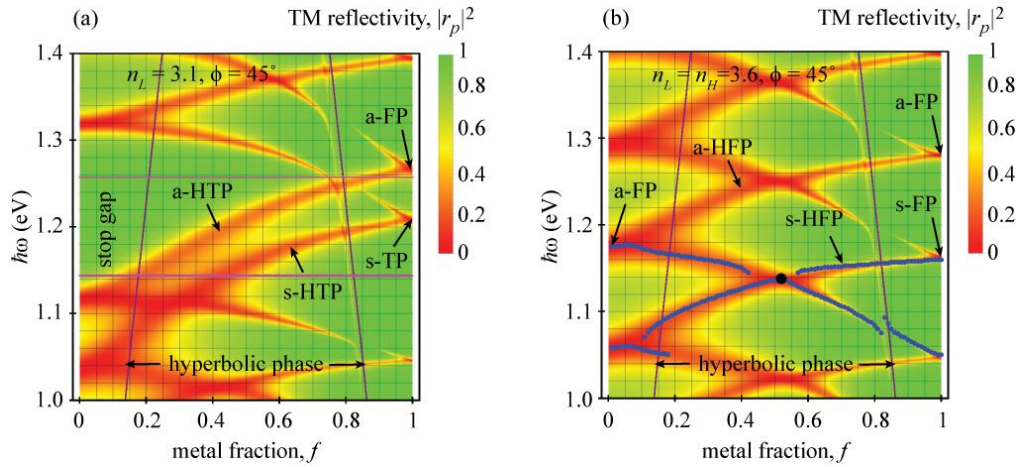
Fig. 4.4 Splitting of HTPs and formation of HFP resonances. (a) TM reflectivity spectrum, $|r_p|^2$, at intermediate contrast in the DBR ($n_l = 3.1$), (b) The same at no contrast in the DBR.

Hyperbolic Fabry-Perot Resonances.

A further decrease of the dielectric contrast of the DBR causes the stop gap to collapse (see Fig. 4.4(b)) and there are no resonances of TP character. All of the resonances evolve into FP resonances as shown in Fig. 4.4(b). In the extreme metal ($f \approx 1$) and dielectric ($f \approx 0$) phases of

the metasurfaces those resonances correspond to the usual FP modes without TM/TE coupling. Within the hyperbolic phase these resonances correspond to novel hyperbolic Fabry-Perot (HFP) modes whose existence we predict in this chapter for the first time.

To understand the HFP resonances consider a Type II Metacavity, which is composed of a layer of homogeneous material sandwiched between two structures containing uniaxial metasurfaces with reflection coefficients r_{pp} and r_{sp} in TM polarization in response to TM and TE incidence correspondingly and r_{ps} and r_{ss} in TE polarization. In this case the resonance condition can be found from the following equation

$$\begin{pmatrix} A_p \\ A_p r_{pp}^L + A_s r_{sp}^L \\ A_s \\ A_p r_{ps}^L + A_s r_{ss}^L \end{pmatrix} = \begin{pmatrix} e^{i\phi} & 0 & 0 & 0 \\ 0 & e^{-i\phi} & 0 & 0 \\ 0 & 0 & e^{i\phi} & 0 \\ 0 & 0 & 0 & e^{-i\phi} \end{pmatrix} \begin{pmatrix} B_p r_{pp}^R + B_s r_{ss}^R \\ B_p \\ B_p r_{ps}^R + B_s r_{ss}^R \\ B_s \end{pmatrix} \tag{4.6}$$

Eq. (4.6) is structured similarly to Eq. (4.4) and has nontrivial solutions only if

$$\left(r_{pp}^L r_{pp}^R + r_{sp} r_{ps} + \frac{\left(r_{pp}^L r_{sp}^R + r_{sp}^L r_{ss}^R\right)\left(r_{pp}^R r_{ps}^L + r_{ps}^R r_{ss}^L\right)e^{2i\phi}}{1 - r_{ps}^L r_{sp}^R e^{2i\phi} - r_{ss}^L r_{ss}^R e^{2i\phi}} \right) e^{2i\phi} - 1 = 0$$

$$\left(r_{ss}^L r_{ss}^R + r_{ps} r_{sp} + \frac{\left(r_{pp}^L r_{sp}^R + r_{sp}^L r_{ss}^R\right)\left(r_{pp}^L r_{ps}^L + r_{ps}^L r_{ss}^R\right)e^{2i\phi}}{1 - r_{pp}^L r_{pp}^R e^{2i\phi} - r_{sp}^L r_{ps}^R e^{2i\phi}} \right) e^{2i\phi} - 1 = 0 \tag{4.7}$$

As can be seen from Eq. (4.7) the resonances of the metacavities involve co-propagation and multiple coupled reflections of TM and TE polarized waves in a similar, but a more complex form, than the one shown in Fig 4.1(a). We plot the minima of the right-hand side of Eq. (4.7) in Fig. 4.4(b) as set of blue dots and they correspond nicely to the HFP resonance minima in reflectivity $|r_p|^2$ of the structure.

The fields in HFP resonances exhibit unique properties. In Fig. 4.5(a) we show the electric field in the metasurface cavity with parameters indicated by a black dot in Fig. 4.4(b). The field inside of the cavity is a standing wave, with polarization rotating between the sides of the cavity, but being close to linear at any given point inside of the cavity. This is demonstrated by the blue curve in Fig. 4.5(a), which follows the end of the electric field vector through the metacavity at a given moment of time, meanwhile in red the polarization ellipsoids are shown at several locations and demonstrate the close to linear polarization at those points. One can notice an efficient 90° polarization rotation as light passes through this Type II Metacavity.
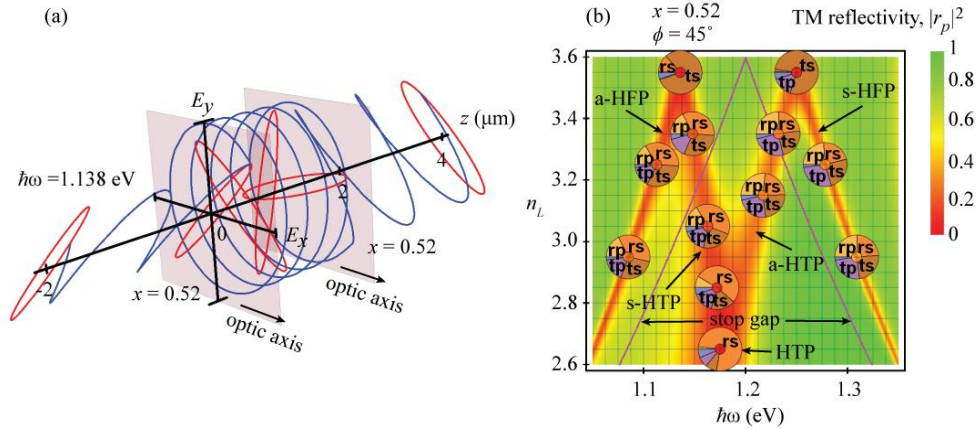
Fig. 4.5 Electric field and power distribution channels in hyperbolic resonances. (a) Electric field at HFP in a Type II Metacavity. (b) Evolution of power distribution in Hyperbolic Metacavities.

In Fig. 4.5(b) we summarize the transition from the HTP resonance to HFP resonance as the contrast in the DBR is reduced (i.e. n_l is increased to $n_l = 3.6$). The pie charts in the figure illustrate the power channels over which the incoming power is distributed for the values of the parameters at which they are shown, with "rp", "rs", "tp" and "ts" being the TM and TE reflections and TM and TE transmissions correspondingly. Absorption is shown as the blue contribution, but never marked by a letter since it is small.

At high contrast (shown in the bottom of Fig. 4.5(b)) the cavity has a broad stopgap and HTP resonance can be seen at $\hbar\omega = 1.18\ eV$. As was described above about 80% of the incoming TM polarized power goes into TE reflection, indicating that HTP-supporting structures can serve as efficient 90° polarization rotation mirrors. As the contrast is reduced the HTP splits and within the resulting s-HTP and a-HTP resonances the power is distributed over all four channels (with exception of absorption which is small). At smaller contrasts the stop gap is not as broad and the split modes leave the stop gap becoming HFP modes in nature. Two other HFP modes are shown on the sides of Fig. 4.5(b). In these modes power also is distributed over all four reflection and transmission channels. They converge and cross with the previously mentioned HFPs and interfere with them. This results in the predominance of TE transmission as indicated at the intersection of the modes (top of Fig. 4.5(b)).

Conclusion

In conclusion, we propose a new class of optical resonators - *metacavities* - and predict that such resonators support novel *hyperbolic resonances*. These hyperbolic optical modes feature unique electromagnetic field distribution within the metacavity, strong TM/TE polarizations coupling and anisotropic dispersion, offering new avenues of photonics research.

Supplementary Material for Chapter 4

Characteristic Matrix Approach. Consider a uniaxial anisotropic medium whose optical axis is in xy-plane at angle ϕ with respect to the x-axis. The dielectric permittivity tensor is

$$\hat{\varepsilon} = \begin{pmatrix} \varepsilon_\parallel \cos^2\phi + \varepsilon_\perp \sin^2\phi & (\varepsilon_\perp - \varepsilon_\parallel)\cos\phi\sin\phi & 0 \\ (\varepsilon_\perp - \varepsilon_\parallel)\cos\phi\sin\phi & \varepsilon_\perp \cos^2\phi + \varepsilon_\parallel \sin^2\phi & 0 \\ 0 & 0 & \varepsilon_\perp \end{pmatrix} = \begin{pmatrix} \varepsilon_{1,1} & \varepsilon_{1,2} & 0 \\ \varepsilon_{2,1} & \varepsilon_{2,2} & 0 \\ 0 & 0 & \varepsilon_\perp \end{pmatrix} \qquad (4.8)$$

The Maxwell equations can be written as $E_z' = -XH_y/\varepsilon_\perp$, and $H_z = XE_y$, where $X = k/k_0$. Also $E_x' = ik_0 H_y - ik^2 H_y/(k_0\varepsilon_\perp)$, $H_y' = ik_0\varepsilon_{1,1}E_x + ik_0\varepsilon_{1,2}E_y$, $E_y' = ik_0 H_x$, $H_x' = -ik_0\varepsilon_{1,2}E_x + ik^2 E_y/k_0$. This can be collected as

$$\frac{\partial}{\partial z}\Psi = ik_0\hat{\Delta}\Psi \qquad (4.9)$$

where $\Psi = (H_y, E_x, E_y, H_x)$ and

$$\hat{\Delta} = \begin{pmatrix} 0 & \varepsilon_{1,1} & \varepsilon_{1,2} & 0 \\ 1 - \dfrac{X^2}{\varepsilon_\perp} & 0 & 0 & 0 \\ 0 & 0 & 0 & -1 \\ 0 & -\varepsilon_{1,2} & -(\varepsilon_{2,2} - X^2) & 0 \end{pmatrix} \qquad (4.10)$$

The solution has a form $\Psi = \Psi_0 e^{iqz}$, which leads to a characteristic equation

$$\hat{\Delta}\Psi = Q\Psi \qquad (4.11)$$

were $Q = q/k_0$. The eigenvalues are $Q = \pm Q_0 = \pm\sqrt{\varepsilon_\perp - X^2}$ and

$$Q = \pm Q_e = \pm\sqrt{\varepsilon_\parallel - X^2\left(\sin^2\phi + \frac{\varepsilon_\parallel}{\varepsilon_\perp}\cos^2\phi\right)}.$$

From this one can obtain a characteristic matrix $\widehat{M}$ of such an anisotropic layer in the region

$0 < z < d$

$$\widehat{M} = \frac{1}{1 + Y \tan^2 \phi} \left(\widehat{M}_0 + \left(\widehat{M}_{1e} - \widehat{M}_{10} \right) \tan \phi + \widehat{M}_2 \tan^2 \phi \right) \tag{4.12}$$

such that

$$\begin{pmatrix} E_x(z = 0) \\ H_y(z = 0) \\ E_y(z = 0) \\ -H_x(z - 0) \end{pmatrix} = \widehat{M} \cdot \begin{pmatrix} E_x(z - d) \\ H_y(z = 0) \\ E_y(z = d) \\ -H_y(z = d) \end{pmatrix} \tag{4.13}$$

The matrices in Eq. (4.12)

$$\widehat{M}_0 = \begin{pmatrix} \cos(Q_e k_0 d) & -iY Q_e \sin(Q_e k_0 d) & 0 & 0 \\ -\dfrac{i}{Y Q_e} \sin(Q_e k_0 d) & \cos(Q_e k_0 d) & 0 & 0 \\ 0 & 0 & \cos(Q_0 k_0 d) & \dfrac{i}{Q_0} \sin(Q_0 k_0 d) \\ 0 & 0 & iQ_0 \sin(Q_0 k_0 d) & \cos(Q_0 k_0 d) \end{pmatrix} \tag{4.14}$$

$$\widehat{M}_{1,e} = \begin{pmatrix} 0 & 0 & iY Q_e \sin(Q_e k_0 d) & Y \cos(Q_e k_0 d) \\ 0 & 0 & -\cos(Q_e k_0 d) & -\dfrac{i}{Q_e} \sin(Q_e k_0 d) \\ \dfrac{i}{Q_e} \sin(Q_e k_0 d) & -Y \cos(Q_e k_0 d) & 0 & 0 \\ \cos(Q_e k_0 d) & -Y Q_e \sin(Q_e k_0 d) & 0 & 0 \end{pmatrix} \tag{4.15}$$

$$\widehat{M}_{1,0} = \begin{pmatrix} 0 & 0 & iY Q_0 \sin(Q_0 k_0 d) & Y \cos(Q_0 k_0 d) \\ 0 & 0 & -\cos(Q_0 k_0 d) & -\dfrac{i}{Q_0} \sin(Q_0 k_0 d) \\ \dfrac{i}{Q_0} \sin(Q_0 k_0 d) & -Y \cos(Q_0 k_0 d) & 0 & 0 \\ \cos(Q_0 k_0 d) & -iY Q_0 \sin(Q_0 k_0 d) & 0 & 0 \end{pmatrix} \tag{4.16}$$

$$
\widehat{M}_2 = \begin{pmatrix} Y\cos(Q_0 k_0 d) & -iY^2 Q_0 \sin(Q_0 k_0 d) & 0 & 0 \\ -\dfrac{i}{Q_0}\sin(Q_0 k_0 d) & Y\cos(Q_0 k_0 d) & 0 & 0 \\ 0 & 0 & Y\cos(Q_e k_0 d) & \dfrac{iY}{Q_e}\sin(Q_e k_0 d) \\ 0 & 0 & iYQ_e \sin(Q_e k_0 d) & Y\cos(Q_e k_0 d) \end{pmatrix} \tag{4.17}
$$

where $Y = \dfrac{\varepsilon_\perp}{\varepsilon_\perp - X^2}$.

Polarization Rotation Equations. Consider a coordinate system in which x'-axis is directed along the incidence plane, while x-axis is along the optical axis. The incident wave in different coordinates are related as

$$
\begin{pmatrix} E_{x(0°)}^{inc} \\ E_{x(90°)}^{inc} \end{pmatrix} = \widehat{M}\begin{pmatrix} E_{x'(TM)}^{inc} \\ E_{y'(TE)}^{inc} \end{pmatrix} = \widehat{M}\begin{pmatrix} p_{p0} \\ 0 \end{pmatrix}, \quad \widehat{M} = \begin{pmatrix} \cos\phi & -\sin\phi \\ \sin\phi & \cos\phi \end{pmatrix} \tag{4.18}
$$

At the same time the reflected and transmitted waves can be found as

$$
\begin{pmatrix} E_{x(0°)}^{ref} \\ E_{x(90°)}^{ref} \end{pmatrix} = \begin{pmatrix} -r_p^{0°} & 0 \\ 0 & r_p^{90°} \end{pmatrix}\begin{pmatrix} E_{x(0°)}^{inc} \\ E_{x(90°)}^{inc} \end{pmatrix}, \quad \begin{pmatrix} E_{x(0°)}^{tr} \\ E_{x(90°)}^{tr} \end{pmatrix} = \begin{pmatrix} \dfrac{p_{ps}t_p^{0°}}{p_{p0}} & 0 \\ 0 & p_{ps}t_p^{90°} \end{pmatrix}\begin{pmatrix} E_{x(0°)}^{inc} \\ E_{x(90°)}^{inc} \end{pmatrix} \tag{4.19}
$$

Combining these relationships

$$
\begin{pmatrix} E_{x'(TM)}^{ref} \\ E_{y'(TE)}^{ref} \end{pmatrix} = \begin{pmatrix} -p_{p0}r_p^{\phi} \\ r_s^{\phi} \end{pmatrix} = \widehat{M}^{-1}\begin{pmatrix} E_{x(0°)}^{ref} \\ E_{x(90°)}^{ref} \end{pmatrix} = \widehat{M}^{-1}\begin{pmatrix} -r_p^{0°} & 0 \\ 0 & -r_p^{90°} \end{pmatrix}\widehat{M}\begin{pmatrix} p_{p0} \\ 0 \end{pmatrix} \tag{4.20}
$$

$$
\begin{pmatrix} E_{x'(TM)}^{tr} \\ E_{y'(TE)}^{tr} \end{pmatrix} = \begin{pmatrix} p_{ps}t_p^{\phi} \\ t_s^{\phi} \end{pmatrix} = \widehat{M}^{-1}\begin{pmatrix} E_{x(0°)}^{tr} \\ E_{x(90°)}^{tr} \end{pmatrix} = \widehat{M}^{-1}\begin{pmatrix} \dfrac{p_{ps}t_p^{0°}}{p_{p0}} & 0 \\ 0 & \dfrac{p_{ps}t_p^{90°}}{p_{p0}} \end{pmatrix}\widehat{M}\begin{pmatrix} p_{p0} \\ 0 \end{pmatrix} \tag{4.21}
$$

From which using an identity

$$\widehat{M}^{-1}\begin{pmatrix} a_1 & 0 \\ 0 & a_2 \end{pmatrix}\widehat{M} = \begin{pmatrix} a_1\cos^2\phi + a_2\sin^2\phi & (a_2 - a_1)\sin\phi\cos\phi \\ (a_2 - a_1)\sin\phi\cos\phi & a_1\sin^2\phi + a_2\sin^2\phi \end{pmatrix} \tag{4.22}$$

we obtain Eqns. (4.3).

Chapter 5

Conclusions

In the preceding we have demonstrated several ways in which the fundamental properties of light can be transformed through interaction with nanostructured materials. We have studied the behavior of materials interacting with radiation from oscillating dipoles that emit into the full range of $\vec{k}$ and all polarizations as well as structures that were under the influence of a plane-wave irradiation where the value of $\vec{k}$ and the polarization are fixed. Polarization rotation wherein the spin angular momentum of incident radiation is changed has been explored in unique new structures. We have shown that alterations to the environment on the nano-scale can have enormous impacts on the behavior of electromagnetic radiation as it conforms to those changes.

We offered a theoretical explanation of the experimental work conducted by Dr. Noginova's team at Norfolk State University. We examined the differing behavior of the electric and magnetic dipole transition for Eu^{3+} ions embedded in a polystyrene layer deposited on top of varying thicknesses of both gold and silver. As the height of the dipoles within the layer was random we had to determine the behavior when the height of the dipole was averaged over. This led to our discovery of the "near-field event horizon."

We showed how a structure that on a superficial level seems very familiar, can exhibit unexpected behavior if one examines it in a rigorous fashion. The metamaterial approximation used therein allowed for the examination of simultaneous ENP and ENZ modes which allow for the proposal of quarter wave plate devices of such small thicknesses as to have been previously considered impossible. The fact that these results were confirmed by independent analysis thanks to Matthew LePain lends even more credence to their viability.

We explored the application of these metamaterial structures to the construction of optical metasurface cavities. We examined the possibilities of bounding a DBR with one metasurface and a conventional metal reflector as well as with two metasurfaces. Within these structures we predicted the existence of novel hyperbolic Fabry-Pérot resonances and hyperbolic Tamm plasmons. Low-loss power redistribution was demonstrated through these resonances that support hybridization of TM and TE polarization fields. Through a close examination of the dispersion curves of the system we established that the behaviors described here are not limited to normal incidence but rather have a range of incidence angles over which they exhibit the desired resonances.

The implications of this research stretch from utilizing spectroscopic methods for probing and mapping optical field distributions to the study of organic molecular chirality. By implementing the structures proposed here it is the sincere hope of this researcher that the scientific community might be able to explore the world around us on a scale heretofore inaccessible. At the very least the demonstration of such small scale wave plate devices might cause a disruption to the optics industry allowing for smaller and more efficient devices to come to fruition. Through continued research in the field of photonics the promise of superlensing to

overcome the diffraction limit may prove to be only the first in a wave new technologies that promise to change our lives for the better.

References

1. D. Griffiths, Introduction to Electrodynamics (Pearson Education, 1999)
2. V. Veselago, "The Electrodynamics of Substances With Simultaneously Negative Values of ϵ and μ," Soviet Physics Uspekhi **10**, 509-514 (1968).
3. J. Pendry, "Negative Refraction Makes a Perfect Lens," Phys. Rev. Lett. **85**, 3966-3969 (2000).
4. E. M. Purcell, "Spontaneous Emission Probabilities at Radio Frequencies," Phys. Rev. **69**, 681 (1946).
5. R. A. Shelby, D. R. Smith, S. Schultz, "Experimental Verification of a Negative Index of Refraction," Science 292, 77-79 (2001)
6. D. R. Smith, W. J. Padila, D. C. Vier, S. C. Nemat-Nasser, S. Schultz, "Composite Medium with Simultaneously Negative Permeability and Permittivity," Phys. Rev. Lett. 84, 4184-4187 (2000)
7. J. B. Pendry, A. J. Holden, D. J. Robbins, W. J. Stewart, "Magnetism from Conductors and Enhanced Nonlinear Phenomena," IEEE Transactions on Microwave Theory and Techniques **47**, 2075-2084 (1999)
8. W. Rotman, "Plasma Simulation by Artificial Dielectrics and Parallel-Plate Media," IRE Transactions on Antennas and Propagation **10**, 82-95 (1962)
9. M. Stockman, "Criterion for Negative Refraction with Low Optical Losses from a Fundamental Principle of Causality," Phys. Rev. Lett. **98**, 177404 (2007)
10. S. Zhang, W. Fan, N. C. Panoiu, K. J. Malloy, R. M. Osgood, S. R. J. Brueck, "Experimental Demonstration of Near-Infrared Negative-Index Metamaterials," Phys. Rev. Lett **95**, 137404 (2005)
11. A. J. Hoffman, L. Aledseyev, S. S. Howard, K. J. Franz, D. Wasserman, V. A. Podolskiy, E. E. Narimanov, D. L. Sivco, C. Gmachl, "Negative Refraction in Semiconductor Metamaterials," Nature Materials **6**, 946-950 (2007)
12. A. Poddubny, I. Iorsh, P. Belov, Y. Kivshar, "Hyperbolic Metamaterials," Nature Photonics **7**, 958-967 (2013)
13. R. Fleury, A. Alù, "Cloaking and Invisibility: A Review," Progress In Electromagnetics Research **147**, 171-202 (2014)
14. J. Li, J. B. Pendry, "Hiding Under the Carpet: A New Strategy for Cloaking," Phys. Rev. Lett. **101**, 203901 (2008)
15. K. H. Drexhage, "Interaction of light with monomolecular dye layers," In Progress in Optics **XII**, 162-231 (1974).
16. R. R. Chance, A. Prock, and R. Silbey, "Lifetime of an emitting molecule near a partially reflecting surface," J. Chem. Phys. **60**, 2744 -2748 (1974).
17. W. Lukosz and R. E. Kunz, "Light emission by magnetic and electric dipoles close to a plane interface. I. Total radiated power," JOSA **67**, 1607-1615 (1977).
18. W. Lukosz, "Light emission by magnetic and electric dipoles close to a plane dielectric interface. III. Radiation patterns of dipoles with arbitrary orientation," JOSA **69**, 1495-1503 (1979).
19. R. R. Chance, A. H. Miller, A. Prock, and R. Silbey, "Fluorescence and energy transfer near interfaces: The complete and quantitative description of the Eu^{+3}/mirror systems," J. of Chem. Phys. **63**, 1589-1595 (1975).
20. L. Novotny and B. Hetcht, Principles of Nano-optics, (Cambridge University, 2007).

21. Z. Xi, Y. Lu, P. Yao, W. Yu, P. Wang, and H. Ming, "Controllable directive radiation of a circularly polarized dipole above planar metal surface," Opt. Express **21**, 30327-30335 (2013).

22. P. T. Worthing, R. M. Amos, and W. L. Barnes, "Modification of the spontaneous emission rate of Eu^{3+} ions embedded within a dielectric layer above a silver mirror," Phys. Rev. A **59**, 865-872 (1999).

23. N. Noginova, R. Hussain, M. A. Noginov, J. Vella, and A. Urbas, "Modification of electric and magnetic dipole emission in anisotropic plasmonic systems," Opt. Express, **21**, 23087-23096 (2013).

24. T. H. Taminiau, S. Karaveli, N. F. van Hulst, and R. Zia, "Quantifying the magnetic nature of light emission", Nat. Commun. **3**, 979 (2012).

25. S. Karaveli and R. Zia, "Spectral tuning by selective enhancement of electric and magnetic dipole emission," Phy. Rev. Lett. **106**, 193004 (2011).

26. S. Karaveli and R. Zia, "Strong enhancement of magnetic dipole emission in a multilevel electronic system," Opt. Lett. **35**, 3318-3320 (2010).

27. S. Karaveli, A. J. Weinstein, and R. Zia, "Direct modulation of lanthanide emission at sub-lifetime scales," Nano Letters **13**, 2264-2269 (2013).

28. X. Ni, G. V. Naik, A. V. Kildishev, Y. Barnakov, A. Boltasseva, and V. M. Shalaev, "Effect of metallic and hyperbolic metamaterial surfaces on electric and magnetic dipole emission transitions," Appl. Phys. B **103**, 553-558 (2011).

29. N. Noginova, G. Zhu, M. Mavy, and M. A. Noginov, "Magnetic dipole based systems for probing optical magnetism," J. Appl. Phys. **103**, 07E901 (2008).

30. N. Noginova, Yu. Barnakov, H. Li, and M. A. Noginov, "Effect of metallic surface on electric dipole and magnetic dipole emission transitions in Eu^{3+} doped polymeric film," Opt. Express **17**, 10767-10772 (2009).

31. R. Hussain, C. Whitefield, C. Carroll, J. Vella, A. Urbas, and N. Noginova, "Emission of electric and magnetic dipoles in plasmonic systems," in CLEO Technical Digest (CLEO, 2012), paper # QM4H.7.

32. S. N. Sheikholeslami , A. García-Etxarri, and J. A. Dionne, "Controlling the Interplay of Electric and Magnetic Modes via Fano-like Plasmon Resonances," Nano Lett. **11**, 3927–3934 (2011).

33. K. Wang, L. Gao, and C. Huang, "Optical properties of the highly ordered Langmuir-Blodgett film of a strongly luminescent Eu(III) complex," J. of Photochem. Photobiol. A: Chem. **156,** 39-43 (2003).

34. J. G. Reifenberger, G. E. Snyder, G. Baym, and P. R. Selvin, ""Emission polarization of europium and terbium chelates," J. Phys. Chem. B **107**, 12862 (2003).

35. J.E. Sipe, "The dipole antenna problem in surface physics: a new approach", Surface Science **105**, 489-504 (1981)

36. G.W. Ford, W.H. Weber, "Electromagnetic interactions of molecules with metal surfaces", Physics Reports **113**, 195-287 (1984)

37. M. Durach, A. Rusina, V. I. Klimov, M. I. Stockman, "Nanoplasmonic renormalization and enhancement of Coulomb interactions," New J. of Phys. **10**, 105011 (2008)

38. R. M. A. Azzam, "Transformation of Fresnel's interface reflection and transmission coefficients between normal and oblique incidence," JOSA **69**, 590-596 (1979).

39. M. Born, E. Wolf, Principles of Optics (Cambridge University Press, 1999).

40. A. V. Kildishev, A. Boltasseva, V. M. Shalaev, "Planar Photonics with Metasurfaces," Science **339**, 1232009, (2013).
41. N. Yu, F. Capasso, "Flat Optics with Designer MetaSurfaces," Nature Materials **13**, 139-150 (2014)
42. Y. Zhao, X.-X. Liu, A. Alù, "Recent Advances on Optical Metasurfaces," Journal of Optics **16**, 123001, (2014)
43. J. Hao, Q. Ren, Z. An, X. Huang, Z. Chen, M. Qiu, L. Zhou, "Optical Metamaterial for Polarization Control," Physical Review A **80**, 023807 (2009).
44. A. Pors, M. G. Nielsen, S. I. Bozhevolnyi, "Broadband Plasmonic Half-Wave Plates in Reflection," Optics Letters **38**, 513-515 (2013)
45. A. Pors, S. I. Bozhevolnyi, "Plasmonic Metasurfaces for Efficient Phase Control in Reflection," Optics Express **21**, 2942-2952 (2013)
46. Z. H. Jiang, L. Lin, D. Ma, S. Yun, D. H. Werner, Z. Liu, T. S. Mayer, "Broadband and Winde Field-of-view Plasmonic Metasurface-enabled Waveplates," Scientific Reports **4**, 7511 (2014).
47. D. Keene, M. Durach, "Hyperbolic Resonances of Metasurface Cavities," Optics Express **23**, 18577-18588 (2015)
48. A. Papakostas, A. Potts, D. M. Bagnall, S. L. Prosvirnin, H. J. Coles and N. I. Zheludev, "Optical Manifestations of Planar Chirality," Physical Review Letters **90**, 107404 (2003)
49. A. Drezet, C. Genet and T. W. Ebbesen, "Miniature Plasmonic Wave Plates," Physical Review Letters **101**, 043902 (2008)
50. Khoo, E. H., E. P. Li and K. B. Crozier, "Plasmonic Wave Plate Based on Subwavelength Nanoslits," Optics letters **36**, 2498-2500 (2011)
51. Y. Zhao, A. Alù, "Manipulating Light Polarization with Ultrathin Plasmonic Metasurfaces," Physical Review B **84**, 205428 (2011).
52. P. Ginzburg, F. J. R. Fortuño, G. A. Wurtz, W. Dickson, A. Murphy, F. Morgan, R. J. Pollard, I. Iorsh, A. Atrashchenko, P. A. Belov, Y. S. Kivshar, A. Nevet, G. Ankonina, M. Orenstein and A. V. Zayats, "Manipulating Polarization of Light with Ultrathin Epsilon-near-zero Metamaterials," Optics Express **21**, 14907-14917 (2013)
53. Slobozhanyuk, A. P., P. Ginzburg, D. A. Powell, I. Iorsh, A. S. Shalin, P. Segovia, A. V. Krasavin, G. A. Wurtz, V. A. Podolskiy, P. A. Belov, A. V. Zayats, "Purcell Effect in Hyperbolic Metamaterial Resonators," Physical Review B **92**, 195127 (2015)
54. Franco Gori, "Measuing Stokes Parameters by Means of a Polarization Grating," Optics Letters, **24**, 584-586 (1999)
55. Uriel Levy, Hyo-Chang Kim, Chia-Ho Tsai, and Yeshaiahu Fainman, "Near-infrared Demonstration of Computer-generated Holograms Implemented by Using Subwavelength Gratings with Space-variant Orientation," Optics Letters **30**, 2089-2091 (2005)
56. G. Zheng, Mühlenbernd, H., Kenney, M., Li, G., Zentgraf, T., S. Zhang, "Metasurface Holograms Reaching 80% Efficiency," Nature Nanotechnology, **10**, 308-312 (2015)
57. L. Marrucci, C. Manzo, D. Paparo, "Optical Spin-to-orbital Angular Momentum Conversion in Inhomogeneous Anisotropic Media," Physical Review Letters, **96**, 163905 (2006).
58. Z. E. Bomzon, G. Biener,V. Kleiner, E. Hasman, "Space-variant Pancharatnam-BerryPhase Optical Elements with Computer-generated Subwavelength Gratings," Optics Letters, **27**, 1141-1143 (2002)
59. A. La Porta, M. D. Wang, "Optical Torque Wrench: Angular Trapping, Rotation, and Torque Detection of Quartz Microparticles," Physical Review Letters **92**, 190801 (2004)

60. F. Pedaci, Z. Huang, M. van Oene, S. Barland, N. H. Dekker , "Excitable Particles in an Optical Torque Wrench," Nature Physics **7**, 259-264 (2011)

61. B. Sturman, E. Podivilov, M. Gorkunov, "Theory of Extraordinary Light Transmission Through Arrays of Subwavelength Slits," Phys. Rev. B **77**,075106 (2008)

62. M. LePain, M. Durach, accepted to Journal of Computational Science Education **7**; arXiv:1508.01861 (2015)

63. J. Elser, R. Wangberg, V. A. Podolskiy, E. E. Narimanov, "Nanowire Metamaterials with Extreme Optical Anisotropy," Applied Physics Letters **89**, 261102 (2006).

64. P. B. Johnson, R. W. Christy, "Optical Constants of the Noble Metals," Physical Review B **6**, 4370-4379 (1972)

65. M. Kaliteevski, I. Iorsh, S. Brand, R. A. Abram, J. M. Chamberlain, A. V. Kavokin, I. A. Shelykh, "Tamm plasmon-polaritons: Possible electromagnetic states at the interface of a metal and a dielectric Bragg mirror". Phys. Rev. B **76**, 165415 (2007).

66. M. E. Sasin, R. P. Seisyan, M. A. Kaliteevski, S. Bbrand, R. A. Abram, J. M. Chamberlain, I. V. Iofsh, I. A. Shelykh, A. Y. Egorov, A. P. Vasil'ev, V. S. Mikhrin, A. V. Kanokin, "Tamm plasmon-polaritons: First experimental observation," Superlattices and Microstructures, **47**, 44 (2010).

67. C. Symonds, G. Lheureux, J. P. Hugonin, J. J. Greffet, L. Laverdant, G. Brucoli, A. Lemaitre, P. Senellart, J. Bellessa, "Confined Tamm plasmon lasers," Nano Letters **13**, 3179 (2013).

68. H. Flayac, G. Pavlovic, M. A. Kaliteevski,I. A. Shelykh, "Electric generation of vortices in polariton superfluids". Phys. Rev. B **85**, 075312 (2012).

69. R. Brückner, M. Sudizius, S. I. Hintschich, H, Fröb, V. G. Lyssenko, K. Leo, "Hybrid optical Tamm states in a planar dielectric microcavity," Phys. Rev. B **83**, 075312 (2011).

70. R. Brückner , M. Sudzius, S. I. Hintschich, H Fröb, V. G. Lyssenko, M. A. Kaliteevski, I. Iorsh, R. A. Abram, A. V. Kavokin, K. Leo, "Parabolic polarization splitting of Tamm states in a metal-organic microcavity," Appl. Phys. Lett. **100**, 062101 (2012)

71. I. Iorsh, P. Panicheva, I. Slovinskii, M. Kaliteevski, "Coupled Tamm plasmons," Technical Phys. Lett., **38**, 351 (2012)

72. M. Durach, A. Rusina, "Transforming Fabry-Perot Resonances into a Tamm mode," Phys. Rev. B **86**, 235312 (2012)

73. O. Gazzano, S. Michaelis de Vasconcellos, K. Gauthron, C. Symonds, J. Bloch, P. Voisin, J. Bellessa, A. Lemaître, P. Senellart, "Evidence for confined Tamm plasmon modes under metallic microdisks and application to the control of spontaneous optical emission," Phys. Rev. Lett. **107**, 247402 (2011).

74. Z. Huang and E. E. Narimanov, "Zeroth-order transmission resonance in hyperbolic metamaterials," Opt. Express **21**, 15020–15025 (2013).

75. A. Pors and S. I. Bozhevolnyi, "Efficient and broadband quarter-wave plates by gap-plasmon resonators," Opt. Express **21**, 2942(2013).

76. A. Pors, M. G. Nielsen, S. I. Bozhevolnyi, "Broadband plasmonic half-wave plates in reflection," Opt. Lett. **38**, 513 (2013)

77. H. N. S. Krishnamoorthy, Z. Jacob, E. E. Narimanov, I. Kretzschmar, V. M. Menon, "Topological transitions in metamaterials," Science **336**, 205 (2012).

78. M. Noginov, M. Lapine, V. Podolskiy, Y. Kivshar, "Focus issue: hyperbolic metamaterials," Opt. Express **21**, 14895 (2013)

79. D. W. Berreman, "Optics in stratified and anisotropic media: 4×4-matrix formulation," JOSA **62**, 502 (1972)
80. M. Durach, D. Keene, "Hyperbolic Tamm Plasmons" In Frontiers in Optics, pp. FTh3E-3. OSA (2014)